# $CO_2$ Conversion at High Current Densities: Stabilization of Bi(III) Containing Electrocatalysts under $CO_2$ Gas Flow Conditions

Iván Zelocualtecatl Montiel[1,2#], Abhijit Dutta[1#*], Kiran Kiran[1], Alain Rieder[1,2], Anna Iarchuk[1,2], Soma Vesztergom[1,3], Marta Mirolo[4], Isaac Martens[4], Jakub Drnec[4], and Peter Broekmann[1,2*]

[1]*Department of Chemistry, Biochemistry and Pharmaceutical Science, University of Bern, Freiestrasse 3, 3012 Bern, Switzerland*

[2]*National Centre of Competence in Research (NCCR) Catalysis, University of Bern, Freiestrasse 3, 3012 Bern, Switzerland*

[3]*Department of Physical Chemistry, Eötvös Loránd University, Pázmány Péter sétány 1/A, 1117 Budapest, Hungary*

[4]*European Synchrotron Radiation Facility (ESRF), 71 Avenue des Martyrs, 38000, Grenoble, France*

[#]*Contributed equally*
[*]*Corresponding authors: abhijit.dutta@unibe.ch (A. Dutta) and*

*peter.broekmann@unibe.ch (P. Broekmann)*

†Electronic supplementary information (ESI) available.

## ABSTRACT

Herein, we demonstrate the superior performance of novel bismuth subcarbonate ($(BiO)_2CO_3$) film catalysts for formate production using a fluidic $CO_2$-fed electrolyzer device. The subcarbonate catalyst readily forms *in situ* from a $CO_2$-absorbing $Bi_2O_3$ precursor material during the $CO_2$ reduction reaction ($CO_2$RR). In 1 mol dm$^{-3}$ KOH electrolyte solution, a maximum Faradaic efficiency of $FE_{formate}$ = 97.4% (corresponding partial current density of formate formation: $PCD_{formate}$ = –111.6 mA cm$^{-2}$) was achieved at a comparably low applied electrolysis potential of –0.8 V *versus* the reversible hydrogen electrode (RHE). Even higher values of $PCD_{formate}$ = –441.2 mA cm$^{-2}$ ($FE_{formate}$ = 62%) were observed at more cathodic potential, –2.5 V *vs.* RHE. As the alkalinity of the liquid electrolyte is further increased (*e.g.*, by using 5 mol dm$^{-3}$ KOH solution), the performance of formate production is boosted beyond $PCD_{formate}$ values of –1 A cm$^{-2}$. Combined X-ray diffraction and Raman spectroscopic investigations demonstrate an extraordinarily high stability of Bi(III) cations in the catalytically active subcarbonate catalyst phase down to cathode potentials of –1.5 V *vs.* RHE. This

stabilization effect can clearly be attributed to the high abundance of gaseous $CO_2$ under the operating conditions of the gas-fed electrolyzer. In the absence of any $CO_2$ supply, however, the reductive Bi(III)→Bi(0) transition already occurs at much milder conditions of –0.3 V *vs.* RHE, as evidenced by *in situ* Raman spectroscopy in $CO_2$-free 1 mol $dm^{-3}$ KOH electrolyte solution. Advanced X-ray diffraction computed tomography (XRD-CT) technique was applied to gain deeper insights into the spatial distribution of the metallic and subcarbonate phases comprising the active composite catalyst layer (CL) during the $CO_2$RR.

## 1. INTRODUCTION

In recent years, the electrochemical conversion of $CO_2$ into higher-value products has been introduced as a promising and technologically feasible approach for mitigating the negative climatic impact of the steadily increasing levels of atmospheric $CO_2$.[1-3] The $CO_2$ reduction reaction ($CO_2$RR) may become not only economically feasible but also truly sustainable if the surplus of renewable energy originating from solar radiation, wind power, and hydroelectric sources is used as energy input to drive the highly endergonic and kinetically hindered $CO_2$ conversion. The overall electrolysis reaction relies on an oxidative splitting of water (*i.e.*, oxygen evolution reaction, OER) through

$$O_2 + 4e^- + 4H^+ \rightleftharpoons 2H_2O \qquad \text{(acidic)} \qquad \text{Eq. 1}$$

or

$$O_2 + 2H_2O + 4e^- \rightleftharpoons 4OH^- \qquad \text{(alkaline)} \qquad \text{Eq. 2}$$

which is coupled to the reductive conversion of $CO_2$ (denoted hereafter $CO_2$RR). In aqueous reaction environments, oxygen ($O_2$) is the only product that forms on the anode side regardless of the anode material used. However, a variety of $CO_2$RR products can be produced on the cathode, including but not limited to carbon monoxide (CO),[4-9] saturated[4, 10-12] and non-saturated hydrocarbons,[11, 13-17] and, alcohols with various chain lengths and energy densities (e.g., methanol,[12, 18-20] ethanol,[16, 21-23] and n-propanol[24]). Formate is another commodity chemical of high value.[25-26] As recently noted by Chen *et al.*,[26] it is the liquid nature of the formate/formic acid product that enables the downstream product separation following primary electrolysis to be conducted with less effort, thus enhancing the profitability of the overall production process. Existing and potential future applications of formate/formic acid concern formic acid fuel

cells,[27-29] related hydrogen storage technologies,[30] the chemical de-polymerization of lignin (biomass valorization),[31] and its usage as a silage additive.[32] Particularly promising are recent developments aimed at coupling $CO_2$ electrolysis with approaches transforming formate into higher alcohols through biotechnological means, thus opening groundbreaking venues of future ($CO_2$→formate) valorization.[33]

Not only are catalysts essential to accelerate the intrinsically slow $CO_2$RR, they are also required for a selective $CO_2$ transformation, directing the electrolysis toward the targeted product (*e.g.*, formate) and minimizing the parasitic hydrogen evolution reaction (HER) that is typically superimposed on the $CO_2$RR in aqueous reaction environments. Depending on the solution pH, the HER can be fed either through reductive water splitting

$$2H_2O + 2e^- \rightleftharpoons H_2 + 2OH^- \qquad \text{(neutral/alkaline)} \qquad \text{Eq. 3}$$

or by the reduction of protons

$$2H^+ + 2e^- \rightleftharpoons H_2 \qquad \text{(acidic)} \qquad \text{Eq. 4}$$

It has been shown that both the chemical nature of the catalyst material[34] and its morphology on various length scales[35-36] dictate the resulting $CO_2$RR product distribution. The catalyst porosity has been demonstrated to be particularly important for consecutive multi-proton/multi-electron reactions, e.g., the electrosynthesis of higher hydrocarbons and alcohols from $CO_2$, where the accumulation of key intermediates (*e.g.*, CO) in confined reaction spaces of porous catalysts and related local pH effects determine the resulting $CO_2$RR product distribution.[10, 37] However, a weaker impact of mesoscale porosity on the $CO_2$RR product distribution has been reported for coupled electron/proton transfer reactions of reduced complexity, *e.g.*, the formation of formate/formic acid [38] from $CO_2$ according to

$$CO_2 + H_2O + 2e^- \rightleftharpoons HCOO^- + OH^- \qquad \text{(neutral/alkaline)} \qquad \text{Eq. 5}$$

Since the pioneering work by Hori *et al.*,[34] it has been known that particular oxophilic materials, *e.g.*, Sn,[39-43] Pb,[44] Cd,[45] Tl, and In,[46] favor $CO_2$RR pathways toward formate production. However, debate continues regarding the mechanistic role of the respective metal oxides, which are either formed *in situ* during electrolysis, or are applied directly as the catalyst (precursor).[39-42] Advanced *operando* techniques, e.g., vibrational[39, 47-49] and X-ray absorption spectroscopy,[48-50] have been successfully employed to gain deeper mechanistic insight into the electrolysis time,

current density, and potential-dependent activation of $CO_2$RR catalysts under operating conditions.[39, 51] A recent example is based on the use of oxidic bismuth electrocatalysts,[38, 52-53] which had already demonstrated superior selectivities toward formate production in classical H-type cell testing environments, with Faradaic efficiencies (*FE*s) exceeding 95% within an extraordinarily (approximately 1.1 V)[38, 54] wide potential window.

For a $CO_2$-saturated 0.5 mol dm$^{-3}$ $KHCO_3$ electrolyte solution, a combination of electrochemical analysis and *operando* Raman spectroscopy during $CO_2$RR revealed the coupling of two potential-dependent $CO_2$RR pathways as the origin of this superior catalytic performance.[38] At low applied overpotentials (–0.3 V to –0.6 V *vs.* RHE), the $CO_2$RR was shown to proceed predominantly via the so-called subcarbonate pathway (see Figure 1), where pristine $Bi_2O_3$ precursor undergoes a rapid transformation into a bulk bismuth subcarbonate phase.[38, 55-57] The term "bismuth subcarbonate" refers to a mixed oxide/carbonate compound in which the bismuth is an oxidation state of +3. $(BiO)_2CO_3$ is formed through partial exchange of $O^{2-}$ by $CO_3^{2-}$ anions through the reaction of the oxidic precursor with gaseous or dissolved $CO_2$. With the aid of *operando* Raman spectroscopy, Dutta *et al.* could identify the $(BiO)_2CO_3$ subcarbonate phase as the active catalyst under these experimental conditions.[38] However, at electrolysis potentials more negative than –0.6 V *vs.* RHE, the formed $(BiO)_2CO_3$ phase underwent a reductive transformation into metallic Bi, resulting in even higher partial current densities of formate formation ($PCD_{formate}$), *i.e.*, reaching a remarkable value of –85 mA cm$^{-2}$ at –1.6 V *vs.* RHE.[38] In the presence of metallic Bi, the $CO_2$RR proceeds via the Bi-O pathway (Figure 1).[57] At first glance, these results seem to suggest that the so-called subcarbonate reaction pathway of formate formation remains limited to artificial experimental conditions, *e.g.*, to those realized in H-type cell configurations. These conditions have only limited practical relevance for gas-fed electrolyzer systems. In gas-fed electrolyzers the rate of $CO_2$RR is not limited by slow $CO_2$ mass transport, and as a consequence, much higher applied overpotentials (or current densities) can be achieved, while still maintaining high formate selectivity.[54-55, 58]

In the present study, we demonstrate that an accelerated mass transport of gaseous $CO_2$ not only boosts the formate production to values beyond $PCD_{formate} = -1$ A cm$^{-2}$ but can also lead to a substantial stabilization of subcarbonate phases beyond the stability regime observed in classical $CO_2$RR test environments.[38] Our experimental results strongly suggest that observations previously made using H-type cell configurations cannot simply be transferred to experimental

conditions realized in practical gas-fed electrolyzers. This conclusion is particularly relevant for the potential-dependent phase behavior of the used non-metallic $CO_2RR$ catalyst which, as will be demonstrated hereinafter, depends not only on the applied electrode potential but also on the actual $CO_2$ gas supply.

## 2. EXPERIMENTAL

*Fabrication of the gas diffusion electrode (GDE)* – The initial catalyst preparation starts with repetitive Bi foam electrodeposition following established synthesis protocols based on the dynamic hydrogen bubble template (DHBT) metal deposition approach (see Figure S1).[38] For metal foaming, galvanostatic Bi deposition ($j_{geo}$ = –3.0 A cm$^{-2}$) was performed in 100 cm$^3$ of 1.5 mol dm$^{-3}$ $H_2SO_4$ supporting electrolyte (prepared from 96% $H_2SO_4$, ACS grade, Sigma-Aldrich) containing 20 mmol dm$^{-3}$ ammonium bismuth citrate ($C_{12}H_{22}BiN_3O_{14}$, Sigma-Aldrich, purity ≥ 99.5%) as the Bi source. The used three-electrode configuration consisted of a double junction Ag | AgCl | 3 mol dm$^{-3}$ KCl reference electrode (Metrohm), a bright Pt anode (50 mm × 20 mm foil), and a Cu foil support (1 cm$^2$ geometric surface area) acting as the cathode. After completion of the metal foam deposition, the Bi-foam@Cu-foil samples were transferred to a vial containing 3 cm$^3$ of isopropanol (iPrOH, BASF SE, assay ≥ 99.0%) and then ultrasonicated until the porous foam material was completely removed from the Cu foil and dispersed in the iPrOH. Metallic Bi powders were obtained through evaporation of the solvent at 50 °C for 12 hours. To prepare the catalyst ink, 55 mg of the Bi powder was redispersed in a mixture of 19.5 cm$^3$ iPrOH and 0.5 cm$^3$ Nafion perfluorinated resin solution (~5 wt% Nafion in a mixture of lower aliphatic alcohols and 15-20 wt% water, purchased from Sigma-Aldrich), followed by 30 min of sonication at room temperature.

To fabricate the GDE, 17 cm$^3$ of the catalyst ink was spray-coated on the surface (6.3 cm × 6.3 cm) of a commercial gas diffusion layer (GDL, Freudenberg H23C8) via a hand-held airbrush pistole (Master Airbrush, G233) propelled by nitrogen gas (99.999%, Carbagas, Switzerland). The catalyst ink was dried with the assistance of vacuum applied to the backside of the GDL during the ink spray-coating process. The expected (nominal) Bi mass loading of $m_{Bi}$ = 1.17 mg cm$^{-2}$ agrees well with the experimental value obtained by inductively coupled plasma mass spectrometry (ICP-MS; $m_{Bi}$ = 1.06 mg cm$^{-2}$).

The used H23C8-GDL reveals a characteristic bilayer structure composed of a supporting carbon fibrous layer (CFL) and a terminating microporous layer (MPL) on which the catalyst layer (CL) is deposited. MPLs are typically made hydrophobic by the manufacturer, e.g., via coating with polytetrafluoroethylene as a water-repelling agent, to minimize electrolyte flooding into deeper layers of the GDL, which may lead to an undesired blockage of $CO_2$ transport to the active catalyst sites during extended electrolyzer operation. The structural and physical characteristics of the H23C8-GDL are detailed in Figure S2. The most important feature of the used H23C8-GDL is the absence of cracks inside the MPL, which might facilitate massive permeation of liquid electrolyte into the GDL during the operation of the fluidic gas-fed electrolyzer.

For further use, pieces (6.3 cm × 6.3 cm) of these prepared GDEs (denoted ap-Bi@GDEs) were cut into smaller segments (2 cm × 2 cm) by a punching blade. For further activation, the ap-Bi@GDEs were subjected to 6 hours of in-air thermal annealing in a tube furnace (Nabertherm, Germany) at a temperature of 350 °C. The obtained oxidic layer is denoted as ap-$Bi_2O_3$@GDE and represents the starting point for all electrolyses discussed hereinafter. Of note, the transformation of metallic Bi into the corresponding $Bi_2O_3$ does not strongly affect the dendritic nature of the catalyst (precursor), as demonstrated in Figure S3. Similar observations were previously made for the thermal annealing of electrodeposited Cu foams.[10, 36]

*Electrolysis experiments* – All electrolysis experiments were performed in a potentiostatic operation mode utilizing a three-compartment flow cell electrolyzer (ElectroCell, Denmark, see also Figure 2, Figure S4). Cathode and anode compartments were separated from each other by an anion exchange membrane (Sustainion® X37-50 Grade RT Membrane). For the ap-$Bi_2O_3$@GDE, a geometric surface area of 1 $cm^2$ was exposed to the liquid electrolyte. A third compartment, required for the $CO_2$ gas supply, was assembled at the backside of the cathode.

With the aid of a peristaltic pump (LabV1, SHE-LabV1-MC4), anolyte and catholyte were fed through the electrolyzer cell via two separated liquid flow channels at a flow rate of 3.3 $cm^3$ $min^{-1}$. Either 1 mol $dm^{-3}$ or 5 mol $dm^{-3}$ KOH aqueous solution was used as the electrolyte. All solutions were produced using high-purity Milli-Q water (specific resistance of 18.2 MΩ cm, total organic carbon content below 5 ppb, Millipore).

For $CO_2$ electrolysis experiments, humidified $CO_2$ gas (Carbagas, 99.9999%) was fed at atmospheric pressure through the gas channels and the GDE. A gas flow rate of 30–35 $cm^3$ $min^{-1}$ was applied and monitored by a mass flow controller unit (Vögtlin Instruments, GmbH, type

GSC-A9SA-BB2). For selected reference experiments, the gas supply was switched during electrolysis from $CO_2$ to inert Ar gas (99.9999%, Carbagas, Switzerland).

All electrolysis experiments were conducted in a three-electrode configuration consisting of the ap-$Bi_2O_3$@GDE (working electrode, cathode), a Pt foil serving as the counter electrode (anode, geometric surface area of 1.5 $cm^{-2}$), and a leakless Ag | AgCl | 3 mol $dm^{-3}$ KCl reference electrode (eDAQ). To ensure comparability, all potentials measured *vs.* the named reference electrode were converted to the RHE scale according to

$$E_{\mathrm{RHE}} = \mathrm{E}_{\mathrm{Ag\,|\,AgCl\,|\,3\ mol\ dm^{-3}\ KCl}} + 0.210\ \mathrm{V} + (0.0591\ \mathrm{V} \cdot \mathrm{pH}) \qquad \text{Eq. 6}$$

An ECi-200 potentiostat (Nordic Electrochemistry, Denmark) was used to establish potential control during electrolysis. For all measurements, *IR* compensation was applied.

During electrolysis, gaseous products (e.g., $H_2$, CO) were detected and quantified in intervals of 20 min by means of online gas chromatography (GC). For this purpose, the gas flow outlet of the electrolyzer unit was connected to the sampling loop of a gas chromatograph (8610C, SRI Instruments). The GC instrument was equipped with both a packed Hayesep D column and a packed Molesieve 5A column. Argon (99.9999%, Carbagas) served as the carrier gas for GC analysis. To quantify gaseous CO and $H_2$ electrolysis products, a flame ionization detector coupled to a methanizer and a thermal conductivity detector were applied.

The partial current for a given electrolysis product ($I_i$) can be determined from

$$I_i = \frac{x_i \cdot v \cdot F \cdot z}{V_{\mathrm{m}}} \qquad \text{Eq. 7}$$

where $c_i$ refers to the concentration of the formed product in ppm, $z$ represents the number of electrons transferred during the reaction, $F$ = 96485.3 C $mol^{-1}$ is the Faraday constant, $v$ is the volumetric gas flow rate, and $V_m$ represents the molar volume of the gas at 1 atm and room temperature.

The *FE* for a specific gaseous product was calculated by relating the partial current ($I_i$) to the corresponding total current ($I_{total}$) according to

$$FE = \frac{I_i}{I_{\mathrm{total}}} \cdot 100\% \qquad \text{Eq. 8}$$

Non-volatile electrolysis products (e.g., formate), accumulated in the catholyte, were quantified by ion exchange chromatography (IC) using a Metrohm 940 Professional IC Vario instrument

equipped with a Metrosep A Supp 7 column and operated with MagicNet 3.1 software. For selected control experiments, the anolyte was also analyzed with the aim of monitoring possible formate crossover through the anion exchange membrane into the anolyte compartment during electrolysis. For IC analysis, aqueous solutions of 3 mmol $dm^{-3}$ $Na_2CO_3$ and 0.1 mol $dm^{-3}$ $H_2SO_4$ served as the eluent and the suppressor, respectively. The IC instrument was calibrated by injecting known standard formate concentrations in the range of 10-250 ppm prepared by dilution of a 1000 ppm IC standard solution (Sigma-Aldrich). Chromatograms and the corresponding calibration plot are presented in Figure S5. Sample aliquots were diluted (20- to 50-fold) with the eluent prior to IC analysis to inhibit matrix effects arising from the highly concentrated KOH working electrolyte.

*FE* values for non-volatile products were derived from the integrated total charges ($Q_{total}$) of the electrolysis reaction and the partial charges ($Q_i$) corresponding to the formation of a specific product:

$$FE = \frac{Q_i}{Q_{\text{total}}} \cdot 100\% \qquad \text{Eq. 9}$$

The partial charge is calculated according to

$$Q_i = \frac{V_{\text{cath}} \cdot F \cdot z}{M_i} \cdot c_i \qquad \text{Eq. 10}$$

$V_{cath}$ is the total volume of the catholyte circulating in the electrolyzer, $c_i$ denotes the mass concentration of the product *i* (usually expressed in mg $dm^{-3}$ or "ppm"), and $M_i$ is the molar mass of product *i*.

Electrolysis data presented hereinafter were acquired by averaging *FE* and *PCD* values obtained from three independent electrolysis experiments per applied electrolysis potential.

*Structural and compositional characterization of the catalyst – X-ray diffraction (XRD) analyses* were conducted using a STOE Stadi system equipped with a Cu $K_\alpha$ radiation source ($\lambda$ = 0.1540 nm, 40 mA) and operated at 40 keV. X-ray diffractograms were recorded in reflection mode (Bragg–Brentano geometry) in steps of 1° $min^{-1}$ with $2\theta$ values ranging from 0° to 90°. Commercial β-$Bi_2O_3$ (Sigma Aldrich, purity ≥ 99.8 %) and $(BiO)_2CO_3$ (Alfa Aesar, purity > 98.5 %) samples were used as internal references for the peak assignment. The obtained XRD patterns were further analyzed and compared with respective JCPDS (Joint Committee on

Powder Diffraction Standards) data for polycrystalline Bi, β-$Bi_2O_3$, and $(BiO)_2CO_3$ (file no. 85-1331, 78-1793, and 84-1752).

*X-ray diffraction computed tomography (XRD-CT) experiments* were performed at the high-energy beamline ID31 of the European Synchrotron Radiation Facility in Grenoble, France. The X-ray beam was mono-chromatized with a Laue monochromator to an energy of 80 keV and focused to a size of ~ 6×20 $\mu m^2$ (vertical×horizontal) at the sample position. Two-dimensional XRD patterns were collected with a Dectris Pilatus 2 M CdTe detector and radially integrated by pyFAI software.[59] Each slice is reconstructed from 62500 diffraction patterns using a standard back-projection algorithm. 5 slices for each sample are space by 5 μm to cover the whole volume of the catalyst layer.

*Scanning electron microscopy (SEM)/energy-dispersive X-ray (EDX) analysis* was performed with a Zeiss DSM 982 SEM equipped with a Noran SIX NSS200 EDX spectrometer.

The mesoscopic surface morphology of the foam was analyzed by means of *white light interferometry* (Contour GT, Bruker, see Figure3). Vision64 software (Bruker) was used for operating the instrument and for data analysis.

*Contact angle measurements* were conducted using a DSA25 Krüss Advance Drop Shape Analyzer (Krüss GmbH, Hamburg, Germany). Electrodes were mounted on a flat sample stage, and water drops (Milli-Q water, 1.4 μL) were deposited at room temperature.

*Elemental analysis* was performed by means of ICP-MS using a NExION 2000 ICP-MS instrument (Perkin Elmer). For the determination of the catalyst mass loading, GDE samples were dissolved in 3 $cm^3$ of conc. $HNO_3$ (69.3 w%, BASF SE). For the analysis, aliquots of 5 $mm^3$ of this solution were dispersed in 10 $cm^3$ of 2 w% $HNO_3$ solution (2000 times dilution). Sample solutions were measured 6 times each by ICP-MS.

For the post-electrolysis analysis of the electrolyte solution, aliquots of 20 $mm^3$ electrolyte were diluted in 10 $cm^3$ of 2 w% $HNO_3$ solution (500 times dilution). Sample solutions were measured 4 times each by ICP-MS. Repetition measurements served as the basis for the determination of the relative standard deviation (RSD). ICP-MS-related RSD values are typically between 1 and 2%. An extra measuring error of ca. 1.5% needs to be taken into account and is due to the dilution treatment required for certain samples.

*Raman spectroscopic analyses* (*ex situ*) were conducted using a LabRAM HR800 confocal microscope (Horiba Jobin Yvon). Spectral data were collected with Lab Space 3.0 software via

the Raman spectrometer coupled with a confocal microscope (Horiba Jobin Yvon). Calibration was carried out using a silicon wafer standard (520.6 $cm^{-1}$). A large-working-distance objective lens (50X magnification, 8-mm focal length) was applied with a numerical aperture of 0.1 in order to focus a diode-pumped solid-state laser beam (532 nm excitation wavelength, 3 mW power) on the sample and collect the incident and scattered laser light. The details of the *in situ* Raman spectroscopy experiments have been described previously.[38]

To identify the $Bi_{metal}$, $Bi_2O_3$, and $(BiO)_2CO_3$ phases, we used characteristic Raman features at 96 $cm^{-1}$ ($E_g$ mode of $Bi_{metal}$), 313 $cm^{-1}$ ($B_g$ mode ("Bi-O stretch") of $Bi_2O_3$), and 162 $cm^{-1}$ ($A_{1g}$ mode of the carbonate in $(BiO)_2CO_3$), respectively (Figure S6).[60-61]

## 3. RESULT AND DISCUSSION

### 3.1 Characterization of the as-prepared GDEs

Several studies have already demonstrated the superior $CO_2RR$ performance of porous metal foam catalysts[35] electrodeposited with the aid of the DHBT method.[62-68] Herein, we have integrated the DHBT-assisted metal foam electrodeposition approach into a more general and versatile catalyst preparation scheme that is particularly suited for the fabrication of GDEs and that can be used in advanced electrolyzer setups. Owing to instrumental limitations, functionalizing more extended surface areas with the DHBT approach alone remains difficult, considering the required ultra-high (geometric) current densities typically applied for such metal foam electrodeposition (*e.g.*, –3 A $cm^{-2}$).[35, 62-63] As detailed in Figure 3, the new GDE fabrication approach involves the repetitive deposition of metallic foams and their subsequent removal from the planar support electrode by ultrasonication.

Of note, this foam removal method destroys the initially formed primary macro-porosity of the metal foam without affecting the dendritic nature of the electrodeposited material. In particular, for $CO_2RR$ processes in which the primary macroporosity of the foam is less important, *e.g.*, in case of formate production, the excellent catalytic performance and selectivity of the electrodeposited material are preserved, as it was recently shown by Dutta *et al.*[38] This dendritic catalyst material is used for the formulation of catalyst (precursor) inks, which are subsequently spray-coated onto extended gas diffusion layer supports, thereby yielding homogeneous CLs. Further catalyst activation can often be achieved through thermal annealing, *e.g.*, yielding a $Bi_2O_3$ film with a characteristic yellow appearance in the present case (Figure 3).[38]

$Bi_2O_3$ crystallizes in various polymorphic forms, denoted α-$Bi_2O_3$ (monoclinic), β-$Bi_2O_3$ (tetragonal), γ-$Bi_2O_3$ (bcc), δ-$Bi_2O_3$ (cubic), ε-$Bi_2O_3$ (triclinic), and ω-$Bi_2O_3$ (triclinic).[69-72] Amorphous $Bi_2O_3$ has also been reported in the literature.[73] These studies emphasize the necessity of combining XRD analyses with complementary techniques, *e.g.*, Raman spectroscopy/microscopy, that are sensitive to phases lacking any long-range transitional order. Interestingly, the combination of DHBT-assisted bismuth electrodeposition and thermal annealing (*e.g.*, at 350 °C in air) exclusively yields the β-$Bi_2O_3$ phase, which has been described in the literature as the most valuable phase among the known modifications (*e.g.*, for photo-catalytic applications) because it shows the smallest band-gap (~2.58 eV).[69, 73] The synthesis of this phase in a pure form, for instance through wet chemistry (precipitation routes), is often considered difficult in the literature.[69]

Figure 4 depicts top-down SEM and cross-sectional SEM/EDX micrographs as well as representative X-ray diffractograms and Raman data of the as-prepared bismuth oxide film on the GDE (denoted ap-$Bi_2O_3$@GDE). This ap-$Bi_2O_3$@GDE was the starting point for all electrolysis experiments discussed hereinafter. On a macroscopic length scale, the SEM data reveal a homogenous catalyst precursor film (panel a) whereas dendritic features govern the catalyst morphology on a sub-micrometer length scale (panel b). The catalyst (precursor) layer must be porous and permeable for both gases and liquids to enable (i) rapid $CO_2$ transport through the GDL toward the active catalyst sites and (ii) (partial) permeation of the catalyst material by the liquid electrolyte. The inward transport of $CO_2$ and liquid electrolyte into such three-dimensional CL is considered vital for establishing triple-phase boundaries in the CL, thereby facilitating $CO_2$RR.[74-75] As shown by panels c and d of Figure 4, the ap-$Bi_2O_3$ CL has an average thickness of about 28 μm, with the bismuth oxide not penetrating the carbon MPL. The X-ray diffractogram (panel e) and the Raman spectrum (panel f) of the ap-$Bi_2O_3$ CL closely resemble the reference diffractogram and spectrum of β-$Bi_2O_3$.

### 3.2 Electrochemical performance testing

Catalyst performance testing was conducted in 1 mol $dm^{-3}$ and 5 mol $dm^{-3}$ KOH electrolyte solutions using the fluidic electrolyzer system depicted in Figure 2. Unless otherwise stated, electrolysis was carried out for the duration of 1 h with the application of a freshly prepared ap-$Bi_2O_3$@GDE in each case. The catalyst testing results are presented in Figure 5 and confirm the

superior selectivity of the dendritic $Bi_2O_3$ catalyst (precursor) toward formate production that has already been reported for H-type cell experiments.[38, 56]

In 1 mol $dm^{-3}$ KOH solution, the formate efficiency ($FE_{formate}$) increases from an initial value of 72.2% to a maximum of 97.4% as the applied potential was changed from –0.3 V to –0.8 V *vs.* RHE. It is important to note that within a rather broad potential window that spans from –0.6 to –1.2 V *vs.* RHE, the formate efficiency does not fall below 90%. The main (parasitic) by-product of this electrolysis reaction is hydrogen. CO was also detected as a $CO_2$RR by-product but only in trace amounts, never exceeding a Faradaic yield of 2.7% (Table S1). At more negative potentials, the formate efficiency decreases to 62% at –2.5 V *vs.* RHE.

The beneficial effect of using gas-fed electrolyzer systems becomes more obvious when we consider the corresponding PCDs (Figure 5a and Table S2), which greatly exceed those obtained in the H-type cell configuration. In H-type cells such high $CO_2$RR rates cannot be achieved due to reactant mass transport limitations in the $CO_2$-saturated aqueous bicarbonate solution.[38] The $PCD_{formate}$ values steadily increase with the applied potential and reach in the 1 mol $dm^{-3}$ KOH electrolyte solution a value of $PCD_{formate}$ = –441.2 mA $cm^{-2}$ at the most negative applied potential of –2.5 V *vs.* RHE (Table S2). Throughout the entire potential range studied herein, the *FE*s of formate production and the corresponding *PCD* values remain above those of the parasitic HER.

Further improvement of the $PCD_{formate}$ values can be achieved using a 5 mol $dm^{-3}$ KOH aqueous solution as the electrolyte (Figure 5b, Tables S3 and S4). In the present case, a superior formate current density of $PCD_{formate}$ = –1353.4 mA $cm^{-2}$ was found for an applied electrolysis potential of –2.5 V *vs.* RHE. Compared to the results for 1 mol $dm^{-3}$ KOH, the corresponding *FE*s are slightly lower in the 5 mol $dm^{-3}$ KOH solution, reaching a maximum of 85% also at –0.8 V *vs.* RHE. Note that the actual $PCD_{formate}$ and $FE_{formate}$ values might be even higher than those reported in Figure 5b. In particular at high current densities formate crossover through the membrane into the anolyte cannot be neglected anymore.[76] This why the total Faradaic efficiency ($FE_{tot}$), determined from the IC analysis of the catholyte and online GC, remains clearly below 100%, e.g., $FE_{tot}$ = 86.0% at –2.5 V *vs.* RHE (Table S3). Figure S7 demonstrates the detection of formate in the anolyte. The precise quantification of formate in the anolyte stemming from the crossover process is, however, hindered due to possible formate oxidation on the anode. Figure S8 compares the excellent performance of the ap-$Bi_2O_3$@GDE catalyst precursor presented

herein with data published in the literature with an emphasis on gas-fed electrolyzer studies (see also Table S5).

It is important to note that under the harsh experimental conditions applied here, the CLs become structurally unstable (highlighted in red in Figure 5b). This particular form of catalyst degradation is due to the parasitic HER (e.g., $PCD_{H_2}$ = –584.9 mA cm$^{-2}$ at –2.5 V *vs.* RHE), which involves massive gas evolution and $H_2$ bubble formation on and inside the porous CL, leading to structural disintegration of the catalyst film. For this reason, all mechanistic studies discussed hereinafter were performed in the 1 mol dm$^{-3}$ KOH electrolyte, in which CLs remain structurally intact.

3.3 Structural alterations within the CL

To gain insight into the structural and compositional changes occurring to the ap-$Bi_2O_3$@GDE precursor during the $CO_2$RR, processed GDEs were subjected to rigorous *ex situ* XRD and Raman spectroscopic analysis after electrolysis (*post mortem*). To demonstrate the influence of $CO_2$ exposure on the compositional and structural alterations of the catalyst, 1-h electrolyses were performed in two different ways: i.) under a continuous flow of $CO_2$ for the whole duration of the experiment; and ii.) under an initial $CO_2$ flow (30 min) followed by an additional 30 min of electrolysis in a stream of inert Ar gas (see Figure 6). Note that after switching from $CO_2$ to the Ar gas supply, the resulting electrolysis currents stem solely from the HER. For electrolyses that were fully performed under $CO_2$ flow (panels a and c in Figure 6), both XRD and Raman data point to a predominant transformation of the oxidic $Bi_2O_3$ precursor into a bismuth subcarbonate phase according to

$$Bi_2O_3 + CO_2 \rightleftharpoons (BiO)_2CO_3 \qquad \text{Eq. 11}$$

No characteristic features of the original $Bi_2O_3$ phase remained visible in the respective X-ray diffractograms or Raman spectra when the electrolyses were performed in the potential range of –0.6 to –1.5 V *vs.* RHE (panels a and c). To gain more insight into the kinetics of $(BiO)_2CO_3$ formation, selected Raman/XRD analyses were carried out for a series of time-dependent electrolyses performed at –1.0 V *vs.* RHE (Figure S9), which suggested a rapid $Bi_2O_3$ transformation into subcarbonate in the initial stage of $CO_2$ electrolysis. Additional control experiments performed under $CO_2$ gas flow at the open circuit potential (OCP) further revealed

that exposure of the $Bi_2O_3$ precursor to gaseous $CO_2$ in the presence of 1 mol $dm^{-3}$ KOH electrolyte solution is already sufficient to initiate subcarbonate formation (Figure S10). Although neither potential control, nor an ongoing $CO_2RR$ seem to be a prerequisite for the observed $(BiO)_2CO_3$ formation in the alkaline electrolyte solution under $CO_2$ gas flow, $CO_2RR$ clearly accelerates this *in situ* transformation.

A noteworthy difference between the phase transitions occurring under potential control and at OCP is observed in the appearance of metallic Bi, which forms only under reductive conditions (e.g., at –1.0 V *vs.* RHE) but not at OCP (Figure S10). In agreement with this reasoning, metallic Bi is also found as a second (minor) component of the CL in addition to $(BiO)_2CO_3$ in all diffractograms recorded after 1 h of electrolysis in the potential range of –0.6 to –1.5 V *vs.* RHE (panel a and panel c of Figure 6). This experimental finding points to a $CO_2$-mediated (oxo-anion→carbonate-anion) exchange process during the $CO_2RR$, which is superimposed by a (competing) reductive transformation of Bi(III) to Bi(0) according to

$$Bi_2O_3 + 6e^- + 3H_2O \rightleftharpoons 2Bi + 6OH^- \qquad \text{Eq. 12}$$

At lower applied overpotentials (–0.6 to –1.5 V *vs.* RHE), the anion exchange under a continuous $CO_2$ flow is obviously the faster process, whereas the Bi(III) electroreduction to metallic Bi determines the final chemical composition of the CL at higher applied overpotentials. Notably, only $(BiO)_2CO_3$ is detected in the Raman spectroscopy experiments for samples processed at lower applied overpotentials (Figure 6c), with no metallic bismuth present. As recently discussed by Dutta *et al*. on the basis of oxidic Cu foams,[48] the (minor) deviations between XRD and Raman analyses likely originate from the different probing depths of these techniques. Raman spectroscopy is typically considered to be more surface-sensitive than XRD, which probes the entire three-dimensional "bulk" of the porous catalyst film.[48] This would suggest that the surface regions in contact with the aqueous electrolyte are mainly in the subcarbonate form while the more buried "bulk" regions can be both metallic and $(BiO)_2CO_3$. Also, in-plane chemical inhomogeneities in the CL (discussed in detail below) can be partially responsible for observed differences (Figure 6) given the different volume probing depths by different techniques.

$(BiO)_2CO_3$-related features disappear completely from the diffractograms and Raman spectra of GDEs subjected to electrolysis potentials below –1.5 V *vs.* RHE (panels a and c of Figure 6). Our results demonstrate that the subcarbonate reaction pathway of formate formation (Figure 1),

already described for liquid-flow and H-type cell test beds,[38, 54, 77] is also relevant for the $CO_2$RR performed in gas-fed electrolyzer devices. Intriguingly, in the present case, the subcarbonate phase remains stable even at the extremely cathodic potential of –1.5 V *vs.* RHE (Figure 6a and c). This behavior hints to a further stabilization of the $(BiO)_2CO_3$ catalyst in the $CO_2$ gas-fed electrolyzer.

Our findings indicate that the $CO_2$ abundance may be the key factor for the stabilization of Bi(III) in the subcarbonate phase during the $CO_2$RR. $(BiO)_2CO_3$ electroreduction involves the (formal) release of $CO_2$ according to

$$(BiO)_2CO_3 + 6e^- + 2H_2O \rightleftharpoons 2Bi + 6OH^- + CO_2 \qquad \text{Eq. 13}$$

which actually rationalizes the observed cathodic shift of the reduction potential in the presence of gaseous $CO_2$ for the gas-fed electrolyzer. Of note, the bismuth subcarbonate electroreduction can also be formulated by assuming a carbonate anion release according to

$$(BiO)_2CO_3 + 6e^- + 2H_2O \rightleftharpoons 2Bi + 4OH^- + CO_3^{2-} \qquad \text{Eq. 14}$$

The assumed $CO_2$-mediated stabilization of the subcarbonate occurs in the latter case through the carbonic acid/bicarbonate/carbonate/$CO_2$ equilibria in the alkaline electrolyte solution.

To experimentally prove our working hypothesis of a $CO_2$-mediated stabilization of the subcarbonate phase, we performed dedicated control experiments in which 30-min $CO_2$ electrolyses were followed by additional 30-min electrolyses under an Ar gas flow. Under these "inert" conditions, electrolysis continues exclusively through the HER. Panels b and d in Figure 6 depict the corresponding *ex situ* XRD and Raman data of these processed GDEs. The results indeed confirm the complete reductive transformation of $(BiO)_2CO_3$, formed in the initial phase of electrolysis under $CO_2$ supply, into metallic Bi at all applied potentials after the switch from $CO_2$ to an inert Ar gas supply (Figure 6b and d). Corresponding time-dependent experiments (Figure S11) indicate a reduction process that occurs rapidly on the outermost catalyst surface being in contact with aqueous electrolyte (preferentially probed by Raman spectroscopy) with, however, a certain time delay in the three-dimensional bulk of the catalyst material (probed by XRD).

To further support our working hypothesis of a stabilizing effect of $CO_2$, we conducted additional potential-dependent *in situ* Raman spectroscopy experiments in the absence of any $CO_2$ gas supply. Under these conditions $(BiO)_2CO_3$ reduction already occurs in the $CO_2$-free

1 mol $dm^{-3}$ KOH electrolyte solution under relatively mild cathodic conditions, at an applied potential of approximately –0.3 V *vs.* RHE (Figure S12). Of note, corresponding stability Raman experiments using the $Bi_2O_3$ film demonstrate a higher stability of $(BiO)_2CO_3$ against electroreduction compared to the corresponding oxidic precursor (Figure S12), even in the absence of any stabilizing $CO_2$ gas dissolved in the electrolyte or in direct contact with the subcarbonate phase. The observed reduction potential of $Bi_2O_3$ agrees fairly well with the Bi/water Pourbaix diagram depicted in Figure S13.

Our *ex situ* XRD analysis clearly indicates that the subcarbonate formation affects the entire three-dimensional bulk of the $Bi_2O_3$ precursor material. Complementary top-down SEM analysis reveals that both the $CO_2$-mediated transformation of $Bi_2O_3$ and the potential-induced electroreduction of the subcarbonate phase into metallic Bi lead to substantial alterations in film morphology across various length scales (Figure 7). The dendritic appearance, which is characteristic for films of the as-prepared metallic Bi (panels a and b) and annealed $Bi_2O_3$ (panels d and e), disappears in the course of $(BiO)_2CO_3$ formation and is replaced by more compact aggregates of subcarbonate nano-sheets (panels g and k). Further electroreduction of the *in situ*-formed $(BiO)_2CO_3$ at –1.7 V *vs.* RHE leaves more extended micron-sized sheets of metallic Bi behind (panels m and n). Complementary contact angle measurements (panels c and f) hint at a transition from initially hydrophobic to pronounced hydrophilic surface characteristics as a consequence of thermal annealing of the as-prepared metallic Bi (ap-Bi@GDE: $\Theta = 157.7°$). The contact angle of this ap-$Bi_2O_3$@GDE decreased to $\Theta = 28.2°$. Moreover, also the formed bismuth subcarbonate shows pronounced hydrophilic characteristics (pe-$Bi_2O_3$@GDE: $\Theta = 8.8°$ / -0.6 V *vs.* RHE, $\Theta = 24.0°$ / -1.0 V *vs.* RHE, panel i and panel l, respectively). Interestingly, the initial hydrophobic surface properties of the as-prepared Bi were largely recovered after subcarbonate electroreduction back into metallic Bi (denoted pe-Bi@GDE: $\Theta = 144.9°$, after electrolysis at –1.7 V *vs.* RHE, panel o), although the film morphology showed substantial changes, *e.g.*, compared to the as-prepared dendritic Bi.

These contact angle analyses suggest a facile electrolyte permeation of the three-dimensional structure of the CL when the oxidic $Bi_2O_3$ precursor is brought into contact with the aqueous electrolyte. It can be further assumed that such catalyst wetting is sustained even if the oxidic catalyst precursor is transformed into the hydrophilic subcarbonate phase during the $CO_2$RR. To probe the extent to which the interior of the micrometer-thick CL is wetted by the alkaline

electrolyte, we applied cross-sectional SEM/EDX analysis, with a focus on potassium concentration profiles along the surface normal (Figure 8). The exclusive source of potassium cations is the KOH electrolyte solution; therefore, the presence of potassium cations in the GDE serves as a "chemical fingerprint" for the permeation of the CL with electrolyte, and further points to an (undesired) electrolyte flooding into deeper layers of the GDE. This approach represents an extension of the recently developed analysis technique applied for post-electrolysis visualization of potassium carbonate precipitates in the GDE interior.[78] Indeed, the K-EDX mapping suggests complete wetting of the $Bi_2O_3$ precursor layer, the formed subcarbonate, and the metallic bismuth layer down to the MPL (see Figure 8h and 8l). Of note, our above considerations of the wetting characteristics are based solely on (post-electrolysis) *ex situ* contact angle measurements and neglect additional electrocapillary effects under potential control, which might transform an intrinsically hydrophobic material (*e.g.*, metallic Bi film) into a more hydrophilic one. The extent to which the electrolyte is expelled from the CL after the Bi(III) reduction into Bi metal takes place cannot be ultimately determined by the *ex situ* measurements presented herein.

Interestingly, after electrolyses, potassium is also detected inside the MPL of the GDE (Figure 8h and 8l). This observation indicates a partial electrolyte permeation of the MPL during the $CO_2$RR. However, considering the observed high *PCD*s and *FE*s of formate production at these applied electrolysis potentials (see also Figure 5a), it appears unlikely that the micropores of the MPL (Figure S2) would become completely blocked by the electrolyte. The $CO_2$ gas supply through the micropores of the GDL toward the CL is still apparently sufficient, and it is likely that the electrolyte, entering the MPL and the fibrous layer during electrolyzer operation perspirates out of the electrolyzer with the outward $CO_2$ gas stream. Such electrolyte perspiration typically prevents massive electrolyte flooding and complete blockage of the micropores, which would result in substantial $CO_2$RR performance losses.

As a consequence of the described phase transitions, the CL also experiences a further structural alteration in film thickness. Cross-sectional SEM analysis reveals a substantial decrease in CL thickness occurring with subcarbonate formation at –1.0 V *vs.* RHE and $Bi_2O_3$ reduction to metallic Bi at –1.7 V *vs.* RHE (Figure 8a,e,i). The film thickness decreases from an initial value of ~28 μm (ap-$Bi_2O_3$@GDE) to ~12 μm (pe-($BiO_2$)$CO_3$@GDE) and ~10 μm (pe-Bi@GDE). However, complementary ICP-MS analyses of the electrolyte to which the CL was exposed

during electrolysis reveal only a minor loss (< 3%) of catalyst material in the liquid electrolyte (Figure S14), which cannot account for the thickness changes observed in the cross-sectional SEM analysis (Figure 8a,e,i). From this comparison, it can safely be concluded that the density of the CL increases during the transformation of $Bi_2O_3$ into either $(BiO)_2CO_3$ or metallic Bi. This substantial structural alteration obviously does not compromise the facile transport of $CO_2$ through the GDL into the CL (see Figure 5a).

To better understand the differences observed between XRD and Raman spectroscopy (Figure 6), and to gain information on the heterogeneous distribution of $(BiO)_2CO_3$ and metallic Bi in the CL, a series of X-ray diffraction computed tomography (XRD-CT) scans have been collected for samples that were made subject to electrolysis at different potentials. By using this technique[79-80], we can image the chemical composition with relatively high spatial resolution (40 μm) in the whole bulk of the sample. The maps in Figure 9 represent the location of the $(BiO)_2CO_3$ (left column) and metallic Bi (right column) in the CL after 1 hour of $CO_2$RR at increasing cathodic potentials, from –1.0 V to –1.8 V *vs.* RHE for each sample. To derive the concentration profile of $(BiO)_2CO_3$ and metallic Bi as a function of depth, the intensities of the (1,0,3) and (0,1,3) peaks at $2\theta = 3.01°$ for $(BiO)_2CO_3$, and that of the (2,–1,0) peak at $2\theta = 3.91°$ for Bi were integrated in the XRD pattern corresponding to each voxel. The result confirms that the distribution of the phases is rather homogeneous as a function of the CL depth. The coexistence of $(BiO)_2CO_3$ and metallic Bi in the same positions in the GDE is highlighted in Figure 9, with a general increase in the metallic phase at the expense of the carbonate phase for $CO_2$RR at lower potentials. A relatively higher concentration of metallic Bi on the CL surface (in contact with the electrolyte) is observed at extreme negative potential (–1.8 V *vs.* RHE). This is in agreement with the Raman and *ex-situ* XRD measurements showing the preferential subcarbonate phase formation on the same CL-electrolyte interface at lower $CO_2$RR potentials, even though both phases are present in the bulk. The interesting observation that the phases in the bulk are mixed and, therefore, not in thermodynamic equilibrium, can likely be explained by diffusion effects occurring in the CL that lead to uneven potential distribution and a strong in-plane phase inhomogeneity. The potential distribution on the surface of the catalyst layer, in contact with the electrolyte solution, is relatively homogeneous, allowing subsequent phase transformations toward the thermodynamic equilibrium. However, the bulk of the CL can be subjected to much larger concentration and potential differences that can lead to the mixing of crystalline phases.

Hints to phase mixing in particular at "intermediate potentials" can clearly be seen in Figure 10, showing (in panels a and b) the phase distribution of $(BiO)_2CO_3$ and Bi, respectively, in a CL sample following 1 hour electrolysis at –1.6 V *vs.* RHE. These maps reveal locations where either one of the phases is completely missing, marked by white ovals, which can only be explained by assuming that these areas were subject to different $CO_2$ concentrations and/or potential. Apart from these areas, the sample contains both phases, mixed with uneven distribution (panel c). In certain regions, the phase transformation proceeded from the surface in contact with the electrolyte to the bulk. This is demonstrated by the line profiles in panel (d), where we plotted the phase distribution and the relative difference along the grey line shown in panel (c). In this area, the Bi phase is much more abundant close to the electrolyte than in the center of the region. As we observe these effects only at larger scales of several hundred microns, areas of smaller scales are likely homogeneous, as supported be SEM measurements, and this explains the relative homogeneity of phases in the out-of-plane direction. These considerations are important in the CL design, as the slow phase mixing can lead to the degradation of catalyst selectivity and may play a role in long-time catalyst deactivation.

## 4. Conclusions and outlook

In this work, we have integrated the DHBT assisted metal foam deposition of $CO_2$RR catalyst materials into a more general preparation scheme for the preparation of gas diffusion electrodes that can be used in gas-fed electrolyzer set-ups. The so-called subcarbonate reaction pathway of $CO_2$-to-formate electroreduction is shown to be prevalent also at high current densities (*e.g.*, $PCD_{\text{formate}} = -207.1$ mA cm$^{-2}$ and $FE_{\text{formate}} = 95.3\%$ at –1.2 V *vs.* RHE) in these gas-fed electrolyzer systems. We have demonstrated that the local abundance of gaseous $CO_2$ during operation of a gas-fed electrolyzer leads to substantial stabilization of the bismuth subcarbonate catalyst in which Bi is present in an oxidation state of +3. The active subcarbonate phase ($(BiO)_2CO_3$) readily forms *in situ*, during $CO_2$RR, from an oxidic $CO_2$-absorbing $Bi_2O_3$ precursor material. Under a continuous $CO_2$ gas flow in the electrolyzer, the $(BiO)_2CO_3$ phase transforms into metallic Bi only under harsh reductive conditions at applied electrolysis potentials more negative than –1.5 V *vs.* RHE, whereas this cathodic transformation occurs in the absence of $CO_2$ under much milder conditions, at –0.3 V *vs.* RHE, as evidenced by *in situ* Raman spectroscopy. After electroreduction of the $(BiO)_2CO_3$ phase into metallic Bi even higher partials

current densities were observed, e.g., a value of $PCD_{formate}$ = –441.2 mA cm$^{-2}$ at –2.5 V *vs.* RHE. Increasing the alkalinity of the liquid electrolyte further (*e.g.*, by using 5 mol dm$^{-3}$ KOH solution) boosts the $PCD_{formate}$-values beyond –1 mA cm$^{-2}$.

Post-electrolysis K-EDX mapping of cross-sectioned GDEs demonstrated complete permeation of the CL with 1 mol dm$^{-3}$ KOH electrolyte solution as a prerequisite for the formation of triple-phase boundaries facilitating $CO_2$RR.

*Ex situ* CT-XRD techniques were applied to GDEs following electrolysis, and confirmed the appearance of heterogeneous composite catalyst films consisting of metallic Bi and $(BiO)_2CO_3$. Relative phase abundances are not only potential-dependent but also show great variance across the sample, which can compromise the long-term stability of the catalyst.

## ASSOCIATED CONTENT

### Supporting Information

AUTHOR INFORMATION

[#]IZM and [#]AD contributed equally to this work

### Corresponding Authors

*abhijit.dutta@unibe.ch
*peter.broekmann@unibe.ch

### Notes

The authors declare no competing financial interests.

## ACKNOWLEDGMENT

This publication was created as part of NCCR Catalysis (grant number 180544), a National Centre of Competence in Research funded by the Swiss National Science Foundation. A.I. acknowledges financial support from the State Secretariat for Education, Research, and Innovation through a Swiss Government Excellence Scholarship for Foreign Scholars. S. Vesztergom acknowledges financial support from the National Research, Development and Innovation Office of Hungary under the grant FK135375.

## Figure Captions

Figure 1. Reaction pathways of formate formation postulated for bismuth-type catalysts. a) Subcarbonate pathway involving the *in situ* formation of $(BiO)_2CO_3$ from $Bi_2O_3$. b) Bi-O pathway over metallic Bi catalysts.

Figure 2. a) Fluidic cathode configuration used in this study. b) Exploded view of the flow cell electrolyzer. c) Photograph of the assembled electrolyzer setup.

Figure 3. Individual preparation steps required for the fabrication of the GDE coated with the $Bi_2O_3$ film (denoted ap-$Bi_2O_3$@GDE) serving as the catalyst precursor.

Figure 4. a–b) Top-down SEM micrographs of ap-$Bi_2O_3$@GDE. c–d) Cross-sectional SEM and EDX mapping of ap-$Bi_2O_3$@GDE. e) X-ray diffractogram of ap-$Bi_2O_3$@GDE including references for β-$Bi_2O_3$. f) Representative Raman spectrum of the ap-$Bi_2O_3$@GDE.

Figure 5. a) Potential-dependent product distribution of potentiostatic $CO_2$ electrolyses performed in 1 mol $dm^{-3}$ KOH aqueous electrolyte. The data are represented as plots of FE values or corresponding (partial) current densities *versus* the applied electrolysis potential (*E vs.* RHE). Of note, the applied potentials are *IR*-compensated. b) Data set obtained for electrolysis conducted in 5 mol $dm^{-3}$ KOH aqueous electrolyte. Electrolysis results for which the catalyst undergoes structural degradation (mechanical instability under massive hydrogen evolution) are highlighted in red. Numerical data for this figure are presented in Tables S1–S4.

Figure 6. a) *Ex situ* X-ray diffractograms recorded after 60 min of potentiostatic electrolysis in 1 mol $dm^{-3}$ KOH solution under a continuous $CO_2$ gas flow; the *IR*-compensated electrolysis potentials are indicated next to the diffractograms. b) Corresponding X-ray diffractograms of catalyst films subjected to 30 min of electrolysis under a $CO_2$ flow followed by an additional 30 min of electrolysis under an inert Ar gas flow. c) *Ex situ* Raman spectra recorded after 60 min of potentiostatic electrolysis in 1 mol $dm^{-3}$ KOH solution under a continuous $CO_2$ gas flow (corresponding to panel a). d) Raman spectra of catalyst films subjected to 30 min of electrolysis under a $CO_2$ flow followed by an additional 30 min of electrolysis under an inert Ar gas flow (corresponding to panel b). Diffractogram and Raman spectroscopy features corresponding to $Bi_2O_3$, $(BiO)_2CO_3$, and metallic Bi are highlighted in red, blue, and green, respectively.

Figure 7. Top-down SEM inspection and corresponding contact angle measurements of the catalyst (precursor) layers. a–c) As-prepared porous metallic Bi film (denoted ap-Bi@GDE). d–f) As-prepared $Bi_2O_3$ film on the GDL after thermal annealing (denoted ap-$Bi_2O_3$@GDE). g–i) Post-electrolysis (pe) inspection of the CL after 60 min of electrolysis at –0.6 V *vs.* RHE (denoted pe-$(BiO)_2CO_3$@GDE). j–l) Results obtained after 60 min of electrolysis at –1.0 V *vs*. RHE. m–o) Results obtained after 60 min of electrolysis at –1.7 V *vs*. RHE (denoted pe-Bi@GDE).

Figure 8. Representative cross-sectional SEM and EDX analyses of the GDEs. a–d) Data for the ap-$Bi_2O_3$@GDE sample (after thermal annealing of the metallic Bi sample). e–h) Post-electrolysis data for a sample subjected to 60 min of electrolysis in 1 mol $dm^{-3}$ KOH electrolyte at –1.0 V *vs*. RHE; this sample is representative of a predominant presence of the subcarbonate phase. i–l) Post-electrolysis data for a sample subjected to 60 min of electrolysis in 1 mol $dm^{-3}$ KOH at –1.7 V *vs*. RHE; this sample is representative of a predominant presence of the metallic Bi phase.

Figure 9. XRD-CT scans of the catalyst layer after $CO_2$RR (1 h) at various potentials. The left column shows the distribution of $(BiO)_2CO_3$ in different depths and corresponding depth profiles determined at the selected areas of the sample. The right column shows the same for Bi metal phase.

Figure 10 The in-plane distribution of $(BiO)_2CO_3$ (a) and Bi (b) of CL after $CO_2$RR (1 h) at -1.6V *vs.* RHE. The inhomogeneous nature of the phase distribution is highlighted in (c) by showing the Bi/$(BiO)_2CO_3$ ratio. Plot (d) presents line profiles along the grey line in (a), (b) and (c).

# References


1. Appel, A. M.; Bercaw, J. E.; Bocarsly, A. B.; Dobbek, H.; DuBois, D. L.; Dupuis, M.; Ferry, J. G.; Fujita, E.; Hille, R.; Kenis, P. J. A.; Kerfeld, C. A.; Morris, R. H.; Peden, C. H. F.; Portis, A. R.; Ragsdale, S. W.; Rauchfuss, T. B.; Reek, J. N. H.; Seefeldt, L. C.; Thauer, R. K.; Waldrop, G. L., Frontiers, Opportunities, and Challenges in Biochemical and Chemical Catalysis of $CO_2$ Fixation. *Chem. Rev.* **2013,** *113* (8), 6621-6658.

2. Whipple, D. T.; Kenis, P. J. A., Prospects of $CO_2$ Utilization via Direct Heterogeneous Electrochemical Reduction. *J. Phys. Chem. Lett.* **2010,** *1* (24), 3451-3458.

3. Karl, T. R.; Trenberth, K. E., Modern Global Climate Change. *Science* **2003,** *302* (5651), 1719-1723.

4. Hori, Y.; Kikuchi, K.; Suzuki, S., Production of CO and $CH_4$ in Electrochemical Reduction of $CO_2$ at Metal-Electrodes in Aqueous Hydrogencarbonate Solution *Chem. Lett.* **1985,** (11), 1695-1698.

5. Dutta, A.; Morstein, C. E.; Rahaman, M.; Cedeño López, A.; Broekmann, P., Beyond Copper in $CO_2$ Electrolysis: Effective Hydrocarbon Production on Silver-Nanofoam Catalysts. *ACS Catal.* **2018**, *8* (9)*,* 8357-8368.

6. Mistry, H.; Choi, Y. W.; Bagger, A.; Scholten, F.; Bonifacio, C. S.; Sinev, I.; Divins, N. J.; Zegkinoglou, I.; Jeon, H. S.; Kisslinger, K.; Stach, E. A.; Yang, J. C.; Rossmeisl, J.; Cuenya, B. R., Enhanced Carbon Dioxide Electroreduction to Carbon Monoxide over Defect-Rich Plasma-Activated Silver Catalysts. *Angew. Chem. Int. Ed.* **2017,** *56* (38), 11394-11398.

7. Hoshi, N.; Kato, M.; Hori, Y., Electrochemical reduction of $CO_2$ on single crystal electrodes of silver Ag(111), Ag(100) and Ag(110). *J. Electroanal. Chem.* **1997,** *440* (1-2), 283-286.

8. Ma, M.; Djanashvili, K.; Smith, W. A., Selective electrochemical reduction of $CO_2$ to CO on CuO-derived Cu nanowires. *Phys. Chem. Chem. Phys.* **2015,** *17* (32), 20861-20867.

9. Ma, M.; Trześniewski, B. J.; Xie, J.; Smith, W. A., Selective and Efficient Reduction of Carbon Dioxide to Carbon Monoxide on Oxide-Derived Nanostructured Silver Electrocatalysts. *Angew. Chem. Int. Ed.* **2016,** *55* (33), 9748-9752.

10. Dutta, A.; Rahaman, M.; Luedi, N. C.; Mohos, M.; Broekmann, P., Morphology Matters: Tuning the Product Distribution of $CO_2$ Electroreduction on Oxide-Derived Cu Foam Catalysts. *ACS Catal.* **2016,** *6* (6), 3804-3814.

11. Dewulf, D. W.; Jin, T.; Bard, A. J., Electrochemical and Surface studies of Carbon-dioxide Reduction to Methane and Ethylene at Copper electrodes in Aqueous-Solutions. *J. Electrochem. Soc.* **1989,** *136* (6), 1686-1691.

12. Hirunsit, P.; Soodsawang, W.; Limtrakul, J., $CO_2$ Electrochemical Reduction to Methane and Methanol on Copper-Based Alloys: Theoretical Insight. *J. Phys. Chem. C* **2015,** *119* (15), 8238-8249.

13. Dinh, C.-T.; Burdyny, T.; Kibria, M. G.; Seifitokaldani, A.; Gabardo, C. M.; García de Arquer, F. P.; Kiani, A.; Edwards, J. P.; De Luna, P.; Bushuyev, O. S.; Zou, C.; Quintero-Bermudez, R.; Pang, Y.; Sinton, D.; Sargent, E. H., $CO_2$ electroreduction to ethylene via hydroxide-mediated copper catalysis at an abrupt interface. *Science* **2018,** *360* (6390), 783-787.

14. Mistry, H.; Varela, A. S.; Bonifacio, C. S.; Zegkinoglou, I.; Sinev, I.; Choi, Y. W.; Kisslinger, K.; Stach, E. A.; Yang, J. C.; Strasser, P.; Cuenya, B. R., Highly Selective Plasma-Activated Copper Catalysts for Carbon Dioxide Reduction to Ethylene. *Nat. Commun.* **2016,** *7* (1), 12123.

15. Hori, Y.; Takahashi, I.; Koga, O.; Hoshi, N., Selective Formation of C2 Compounds from Electrochemical Reduction of $CO_2$ at a Series of Copper Single Crystal Electrodes. *J. Phys. Chem. B* **2002,** *106* (1), 15-17.

16. Hori, Y.; Murata, A.; Takahashi, R.; Suzuki, S., Enhanced Formation of Ethylene and Alcohols at Ambient Temperature and Pressure in Electrochemcial Reduction of Carbondioxide at a Copper Electrode *J. Chem. Soc., Chem. Commun.* **1988,** (1), 17-19.

17. Yano, H.; Shirai, F.; Nakayama, M.; Ogura, K., Efficient electrochemical conversion of $CO_2$ to CO, $C_2H_4$ and $CH_4$ at a three-phase interface on a Cu net electrode in acidic solution. *J. Electroanal. Chem.* **2002,** *519* (1-2), 93-100.

18. Frese, K. W.; Leach, S., Electrochemical Reduction of Carbondioxide to Methane, Methanol, and CO on Ru Electrodes *J. Electrochem. Soc.* **1985,** *132* (1), 259-260.

19. Ohta, K.; Kawamoto, M.; Mizuno, T.; Lowy, D. A., Electrochemical reduction of carbon dioxide in methanol at ambient temperature and pressure. *J. Appl. Electrochem.* **1998,** *28* (7), 717-724.

20. Albo, J.; Irabien, A., $Cu_2O$-loaded gas diffusion electrodes for the continuous electrochemical reduction of $CO_2$ to methanol. *J. Catal.* **2016,** *343*, 232-239.

21. Hoang, T. T. H.; Verma, S.; Ma, S.; Fister, T. T.; Timoshenko, J.; Frenkel, A. I.; Kenis, P. J. A.; Gewirth, A. A., Nanoporous Copper–Silver Alloys by Additive-Controlled Electrodeposition for the Selective Electroreduction of $CO_2$ to Ethylene and Ethanol. *J. Am. Chem. Soc.* **2018,** *140* (17), 5791-5797.

22. Ren, D.; Ang, B. S.-H.; Yeo, B. S., Tuning the Selectivity of Carbon Dioxide Electroreduction toward Ethanol on Oxide-Derived $Cu_xZn$ Catalysts. *ACS Catal.* **2016,** *6* (12), 8239-8247.

23. Ma, S.; Sadakiyo, M.; Luo, R.; Heima, M.; Yamauchi, M.; Kenis, P. J. A., One-Step Electrosynthesis of Ethylene and Ethanol from $CO_2$ in an Alkaline Electrolyzer. *J. Power Sources* **2016,** *301*, 219-228.

24. Rahaman, M.; Kiran, K.; Montiel, I. Z.; Grozovski, V.; Dutta, A.; Broekmann, P., Selective n-propanol formation from $CO_2$ over degradation-resistant activated PdCu alloy foam electrocatalysts. *Green Chem.* **2020,** *22* (19), 6497-6509.

25. Han, N.; Ding, P.; He, L.; Li, Y.; Li, Y., Promises of Main Group Metal–Based Nanostructured Materials for Electrochemical $CO_2$ Reduction to Formate. *Adv. Energy Mater.* **2020,** *10* (11), 1902338.

26. Chen, Y.; Vise, A.; Klein, W. E.; Cetinbas, F. C.; Myers, D. J.; Smith, W. A.; Deutsch, T. G.; Neyerlin, K. C., A Robust, Scalable Platform for the Electrochemical Conversion of $CO_2$ to Formate: Identifying Pathways to Higher Energy Efficiencies. *ACS Energy Lett.* **2020,** *5* (6), 1825-1833.

27. Rice, C.; Ha, S.; Masel, R. I.; Waszczuk, P.; Wieckowski, A.; Barnard, T., Direct formic acid fuel cells. *J. Power Sources* **2002,** *111* (1), 83-89.

28. Rice, C.; Ha, S.; Masel, R. I.; Wieckowski, A., Catalysts for direct formic acid fuel cells. *J. Power Sources* **2003,** *115* (2), 229-235.

29. Zhu, Y.; Ha, S. Y.; Masel, R. I., High power density direct formic acid fuel cells. *J. Power Sources* **2004,** *130* (1), 8-14.

30. Fellay, C.; Dyson, P. J.; Laurenczy, G., A Viable Hydrogen-Storage System Based On Selective Formic Acid Decomposition with a Ruthenium Catalyst. *Angew. Chem. Int. Ed.* **2008,** *47* (21), 3966-3968.

31. Rahimi, A.; Ulbrich, A.; Coon, J. J.; Stahl, S. S., Formic-acid-induced depolymerization of oxidized lignin to aromatics. *Nature* **2014,** *515* (7526), 249-252.

32. Muck, R. E.; Nadeau, E. M. G.; McAllister, T. A.; Contreras-Govea, F. E.; Santos, M. C.; Kung, L., Silage review: Recent advances and future uses of silage additives. *J. Dairy Sci.* **2018,** *101* (5), 3980-4000.

33. Li, H.; Opgenorth Paul, H.; Wernick David, G.; Rogers, S.; Wu, T.-Y.; Higashide, W.; Malati, P.; Huo, Y.-X.; Cho Kwang, M.; Liao James, C., Integrated Electromicrobial Conversion of $CO_2$ to Higher Alcohols. *Science* **2012,** *335* (6076), 1596-1596.

34. Hori, Y., Electrochemical $CO_2$ Reduction on Metal Electrodes. In *Modern Aspects of Electrochemistry*, Springer: New York, 2008; pp 89-189.

35. Vesztergom, S.; Dutta, A.; Rahaman, M.; Kiran, K.; Zelocualtecatl Montiel, I.; Broekmann, P., Hydrogen Bubble Templated Metal Foams as Efficient Catalysts of $CO_2$ Electroreduction. *ChemCatChem* **2021,** *13* (4), 1039-1058.

36. Dutta, A.; Rahaman, M.; Mohos, M.; Zanetti, A.; Broekmann, P., Electrochemical $CO_2$ Conversion Using Skeleton (Sponge) Type of Cu Catalysts. *ACS Catal.* **2017,** *7* (8), 5431-5437.

37. Liu, X.; Schlexer, P.; Xiao, J.; Ji, Y.; Wang, L.; Sandberg, R. B.; Tang, M.; Brown, K. S.; Peng, H.; Ringe, S.; Hahn, C.; Jaramillo, T. F.; Nørskov, J. K.; Chan, K., pH effects on the electrochemical reduction of $CO_2$ towards C2 products on stepped copper. *Nat. Commun.* **2019,** *10* (1), 32.

38. Dutta, A.; Zelocualtecatl Montiel, I.; Kiran, K.; Rieder, A.; Grozovski, V.; Gut, L.; Broekmann, P., A Tandem ($Bi_2O_3 \rightarrow Bi_{met}$) Catalyst for Highly Efficient ec-$CO_2$ Conversion into Formate: Operando Raman Spectroscopic Evidence for a Reaction Pathway Change. *ACS Catal.* **2021,** *11* (9), 4988-5003.

39. Dutta, A.; Kuzume, A.; Kaliginedi, V.; Rahaman, M.; Sinev, I.; Ahmadi, M.; Cuenya, B. R.; Vesztergom, S.; Broekmann, P., Probing the chemical state of tin oxide NP catalysts during $CO_2$ electroreduction: A complementary operando approach. *Nano energy* **2018,** *53*, 828-840.

40. Dutta, A.; Kuzume, A.; Rahaman, M.; Vesztergom, S.; Broekmann, P., Monitoring the Chemical State of Catalysts for $CO_2$ Electroreduction: An In Operando Study. *ACS Catal.* **2015,** *5* (12), 7498-7502.

41. Sen, S.; Brown, S. M.; Leonard, M.; Brushett, F. R., Electroreduction of carbon dioxide to formate at high current densities using tin and tin oxide gas diffusion electrodes. *J. Appl. Electrochem.* **2019,** *49* (9), 917-928.

42. Lee, S.; Ocon, J. D.; Son, Y.-i.; Lee, J., Alkaline $CO_2$ Electrolysis toward Selective and Continuous HCOO– Production over $SnO_2$ Nanocatalysts. *J. Phys. Chem. C* **2015,** *119* (9), 4884-4890.

43. Zhao, S.; Li, S.; Guo, T.; Zhang, S.; Wang, J.; Wu, Y.; Chen, Y., Advances in Sn-Based Catalysts for Electrochemical $CO_2$ Reduction. *Nano-Micro Lett.* **2019,** *11* (1), 62.

44. García, J.; Jiménez, C.; Martínez, F.; Camarillo, R.; Rincón, J., Electrochemical reduction of $CO_2$ using Pb catalysts synthesized in supercritical medium. *J. Catal.* **2018,** *367*, 72-80.

45. Chen, Z.; Wang, N.; Yao, S.; Liu, L., The flaky Cd film on Cu plate substrate: An active and efficient electrode for electrochemical reduction of $CO_2$ to formate. *J. CO2 Util.* **2017,** *22*, 191-196.

46. Li, J.; Zhu, M.; Han, Y.-F., Recent Advances in Electrochemical $CO_2$ Reduction on Indium-Based Catalysts. *ChemCatChem* **2021,** *13* (2), 514-531.

47. Kuzume, A.; Dutta, A.; Vesztergom, S.; Broekmann, P., Operando Raman spectroscopy: studies on the reactivity and stability of $SnO_2$ nanoparticles during electrochemical $CO_2$ reduction reaction. K. Wandelt (Ed.Encyclopedia of Interfacial Chemistry, Elsevier, Oxford, Encyclopedia of Interfacial Chemistry, Surface Science and Electrochemistry, Elsevier, Amsterdam, **2018**, pp. 217–226.

48. Dutta, A.; Rahaman, M.; Hecker, B.; Drnec, J.; Kiran, K.; Zelocualtecatl Montiel, I.; Jochen Weber, D.; Zanetti, A.; Cedeño López, A.; Martens, I.; Broekmann, P.; Oezaslan, M., $CO_2$ electrolysis – Complementary operando XRD, XAS and Raman spectroscopy study on the stability of $Cu_xO$ foam catalysts. *J. Catal.* **2020,** *389*, 592-603.

49. Zou, Y.; Wang, S., An Investigation of Active Sites for electrochemical $CO_2$ Reduction Reactions: From In Situ Characterization to Rational Design. *Adv. Sci.* **2021,** *8* (9), 2003579.

50. Timoshenko, J.; Roldan Cuenya, B., In Situ/Operando Electrocatalyst Characterization by X-ray Absorption Spectroscopy. *Chem. Rev.* **2021,** *121* (2), 882-961.

51. Dutta, A.; Kiran, K.; Rahaman, M.; Montiel, I. Z.; Moreno-Garcí, P.; Vesztergom, S.; Drnec, J.; Oezaslan, M.; Broekmann, P., Insights from Operando and Identical Location (IL) Techniques on the Activation of Electrocatalysts for the Conversion of $CO_2$: A Mini-Review. *Chimia* **2021,** *75* (9), 733-743.

52. Feng, X.; Zou, H.; Zheng, R.; Wei, W.; Wang, R.; Zou, W.; Lim, G.; Hong, J.; Duan, L.; Chen, H., $Bi_2O_3$/$BiO_2$ Nanoheterojunction for Highly Efficient Electrocatalytic $CO_2$ Reduction to Formate. *Nano Lett.* **2022,** *22* (4), 1656-1664.

53. Deng, P.; Wang, H.; Qi, R.; Zhu, J.; Chen, S.; Yang, F.; Zhou, L.; Qi, K.; Liu, H.; Xia, B. Y., Bismuth Oxides with Enhanced Bismuth–Oxygen Structure for Efficient Electrochemical Reduction of Carbon Dioxide to Formate. *ACS Catal.* **2020,** *10* (1), 743-750.

54. Zhang, Y.; Zhang, X.; Ling, Y.; Li, F.; Bond, A. M.; Zhang, J., Controllable Synthesis of Few-Layer Bismuth Subcarbonate by Electrochemical Exfoliation for Enhanced $CO_2$ Reduction Performance. *Angew. Chem. Int. Ed.* **2018,** *57* (40), 13283-13287.

55. Fan, T.; Ma, W.; Xie, M.; Liu, H.; Zhang, J.; Yang, S.; Huang, P.; Dong, Y.; Chen, Z.; Yi, X., Achieving high current density for electrocatalytic reduction of $CO_2$ to formate on bismuth-based catalysts. *Cell Rep. Phys. Sci.* **2021,** *2* (3), 100353.

56. Shi, Y.; Wen, C. F.; Wu, X.; Zhao, J. Y.; Mao, F.; Liu, P. F.; Yang, H. G., In situ reconstruction of vegetable sponge-like $Bi_2O_3$ for efficient $CO_2$ electroreduction to formate. *Mater. Chem. Front.* **2022**, *6* (8), 1091-1097.

57. Lv, W.; Bei, J.; Zhang, R.; Wang, W.; Kong, F.; Wang, L.; Wang, W., $Bi_2O_2CO_3$ Nanosheets as Electrocatalysts for Selective Reduction of $CO_2$ to Formate at Low Overpotential. *ACS Omega* **2017,** *2* (6), 2561-2567.

58. Lin, J.; Yan, S.; Zhang, C.; Hu, Q.; Cheng, Z., Electroreduction of $CO_2$ toward High Current Density. *Processes* **2022,** *10* (5), 826.

59. Ashiotis, G.; Deschildre, A.; Nawaz, Z.; Wright, J. P.; Karkoulis, D.; Picca, F. E.; Kieffer, J., The fast azimuthal integration Python library: pyFAI. *J. Appl. Crystallogr.* **2015,** *48* (2), 510-519.

60. Reyes-Contreras, A.; Camacho-López, M.; Camacho-López, S.; Olea-Mejía, O.; Esparza-García, A.; Bañuelos-Muñetón, J. G.; Camacho-López, M. A., Laser-induced periodic surface structures on bismuth thin films with ns laser pulses below ablation threshold. *Opt. Mater. Express* **2017,** *7* (6), 1777-1786.

61. Taylor, P.; Sunder, S.; Lopata, V. J., Structure, spectra, and stability of solid bismuth carbonates. *Can. J. Chem.* **1984,** *62* (12), 2863-2873.

62. Shin, H. C.; Dong, J.; Liu, M., Porous Tin Oxides Prepared Using an Anodic Oxidation Process. *Adv. Mater.* **2004,** *16* (3), 237-240.

63. Shin, H. C.; Liu, M., Copper foam structures with highly porous nanostructured walls. *Chem. Mater.* **2004,** *16* (25), 5460-5464.

64. Dutta, A.; Montiel, I. Z.; Erni, R.; Kiran, K.; Rahaman, M.; Drnec, J.; Broekmann, P., Activation of bimetallic AgCu foam electrocatalysts for ethanol formation from $CO_2$ by selective Cu oxidation/reduction. *Nano Energy* **2020,** *68*, 104331.

65. Rudnev, A. V.; Kiran, K.; Cedeño López, A.; Dutta, A.; Gjuroski, I.; Furrer, J.; Broekmann, P., Enhanced electrocatalytic CO formation from $CO_2$ on nanostructured silver foam electrodes in ionic liquid/water mixtures. *Electrochim. Acta* **2019,** *306*, 245-253.

66. Luo, W.; Xie, W.; Mutschler, R.; Oveisi, E.; De Gregorio, G. L.; Buonsanti, R.; Züttel, A., Selective and Stable Electroreduction of $CO_2$ to CO at the Copper/Indium Interface. *ACS Catal.* **2018,** *8* (7), 6571-6581.

67. Luo, W.; Zhang, J.; Li, M.; Züttel, A., Boosting CO Production in Electrocatalytic $CO_2$ Reduction on Highly Porous Zn Catalysts. *ACS Catal.* **2019,** *9* (5), 3783-3791.

68. Kottakkat, T.; Klingan, K.; Jiang, S.; Jovanov, Z. P.; Davies, V. H.; El-Nagar, G. A. M.; Dau, H.; Roth, C., Electrodeposited AgCu Foam Catalysts for Enhanced Reduction of $CO_2$ to CO. *ACS Appl. Mater. Interfaces* **2019,** *11* (16), 14734-14744.

69. Barrera-Mota, K.; Bizarro, M.; Castellino, M.; Tagliaferro, A.; Hernández, A.; Rodil, S. E., Spray deposited β-$Bi_2O_3$ nanostructured films with visible photocatalytic activity for solar water treatment. *Photochem. Photobiol. Sci.* **2015,** *14* (6), 1110-1119.

70. Vila, M.; Díaz-Guerra, C.; Piqueras, J., α-$Bi_2O_3$ microcrystals and microrods: Thermal synthesis, structural and luminescence properties. *J. Alloys Compd.* **2013,** *548*, 188-193.

71. Divya, J.; Shivaramu, N. J.; Purcell, W.; Roos, W. D.; Swart, H. C., Effects of annealing temperature on the crystal structure, optical and photocatalytic properties of $Bi_2O_3$ needles. *Appl. Surf. Sci.* **2020,** *520*, 146294.

72. Liu, G.; Li, S.; Lu, Y.; Zhang, J.; Feng, Z.; Li, C., Controllable synthesis of α-$Bi_2O_3$ and γ-$Bi_2O_3$ with high photocatalytic activity by α-$Bi_2O_3$→γ-$Bi_2O_3$→α-$Bi_2O_3$ transformation in a facile precipitation method. *J. Alloys Compd.* **2016,** *689*, 787-799.

73. Leontie, L.; Caraman, M.; Delibaş, M.; Rusu, G. I., Optical properties of bismuth trioxide thin films. *Mater. Res. Bull.* **2001,** *36* (9), 1629-1637.

74. Lu, Q.; Jiao, F., Electrochemical $CO_2$ reduction: Electrocatalyst, reaction mechanism, and process engineering. *Nano Energy* **2016,** *29*, 439-456.

75. Nesbitt, N. T.; Burdyny, T.; Simonson, H.; Salvatore, D.; Bohra, D.; Kas, R.; Smith, W. A., Liquid–Solid Boundaries Dominate Activity of $CO_2$ Reduction on Gas-Diffusion Electrodes. *ACS Catal.* **2020,** *10* (23), 14093-14106.

76. McCallum, C.; Gabardo, C. M.; O'Brien, C. P.; Edwards, J. P.; Wicks, J.; Xu, Y.; Sargent, E. H.; Sinton, D., Reducing the crossover of carbonate and liquid products during carbon dioxide electroreduction. *Cell Rep. Phys. Sci.* **2021,** *2* (8), 100522.

77. Zhang, M.; Wei, W.; Zhou, S.; Ma, D.-D.; Cao, A.; Wu, X.-T.; Zhu, Q.-L., Engineering a conductive network of atomically thin bismuthene with rich defects enables $CO_2$ reduction to formate with industry-compatible current densities and stability. *Energy Environ. Sci.* **2021,** *14* (9), 4998-5008.

78. Kong, Y.; Hu, H.; Liu, M.; Hou, Y.; Kolivoška, V.; Vesztergom, S.; Broekmann, P., Visualisation and quantification of flooding phenomena in gas diffusion electrodes used for electrochemical $CO_2$ reduction: A combined EDX/ICP–MS approach. *J. Catal.* **2022,** *408*, 1-8.

79. Martens, I.; Vamvakeros, A.; Martinez, N.; Chattot, R.; Pusa, J.; Blanco, M. V.; Fisher, E. A.; Asset, T.; Escribano, S.; Micoud, F.; Starr, T.; Coelho, A.; Honkimäki, V.; Bizzotto, D.; Wilkinson, D. P.; Jacques, S. D. M.; Maillard, F.; Dubau, L.; Lyonnard, S.; Morin, A.; Drnec, J., Imaging Heterogeneous Electrocatalyst Stability and Decoupling Degradation Mechanisms in Operating Hydrogen Fuel Cells. *ACS Energy Lett.* **2021,** *6* (8), 2742-2749.

80. Vamvakeros, A.; Jacques, S. D. M.; Di Michiel, M.; Matras, D.; Middelkoop, V.; Ismagilov, I. Z.; Matus, E. V.; Kuznetsov, V. V.; Drnec, J.; Senecal, P.; Beale, A. M., 5D operando tomographic diffraction imaging of a catalyst bed. *Nat. Commun.* **2018,** *9* (1), 4751.

**Figure 1**

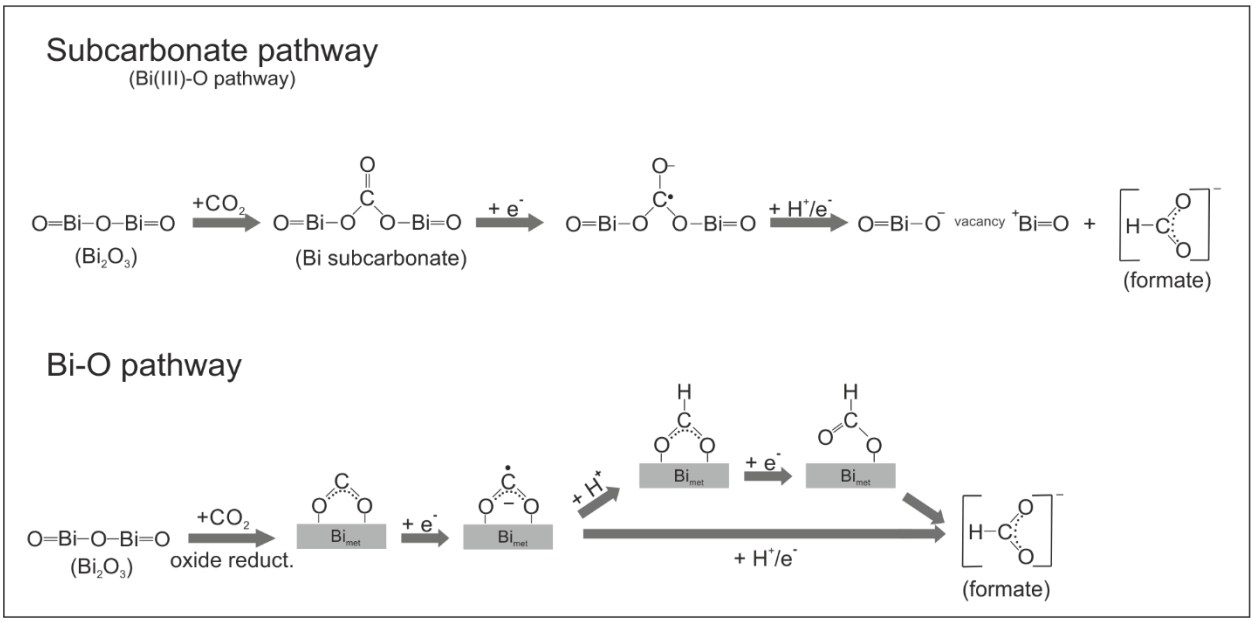
Subcarbonate pathway
(Bi(III)-O pathway)
O=Bi–O–Bi=O
(Bi2O3)
+CO2
O=Bi–O–Bi=O
(Bi subcarbonate)
+ e-
O=Bi–O–Bi=O
+ H+/e-
O=Bi–O vacancy +Bi=O +
(formate)
Bi-O pathway
O=Bi–O–Bi=O
(Bi2O3)
+CO2
oxide reduct.
Bimet
+ e-
Bimet
+ H+
Bimet
+ e-
Bimet
+ H+/e-
(formate)

# Figure 2

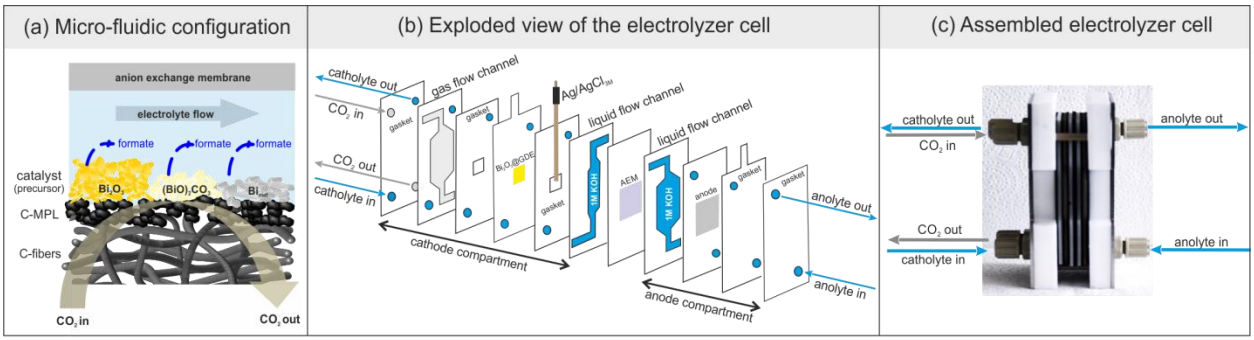
(a) Micro-fluidic configuration
anion exchange membrane
electrolyte flow
formate
formate
formate
catalyst
(precursor)
C-MPL
C-fibers
CO2 in
CO2 out
(b) Exploded view of the electrolyzer cell
catholyte out
CO2 in
CO2 out
catholyte in
gas flow channel
gasket
Ag/AgCl
liquid flow channel
liquid flow channel
AEM
1M KOH
anode
anolyte out
anolyte in
cathode compartment
anode compartment
(c) Assembled electrolyzer cell
catholyte out
CO2 in
CO2 out
catholyte in
anolyte out
anolyte in

# Figure 3

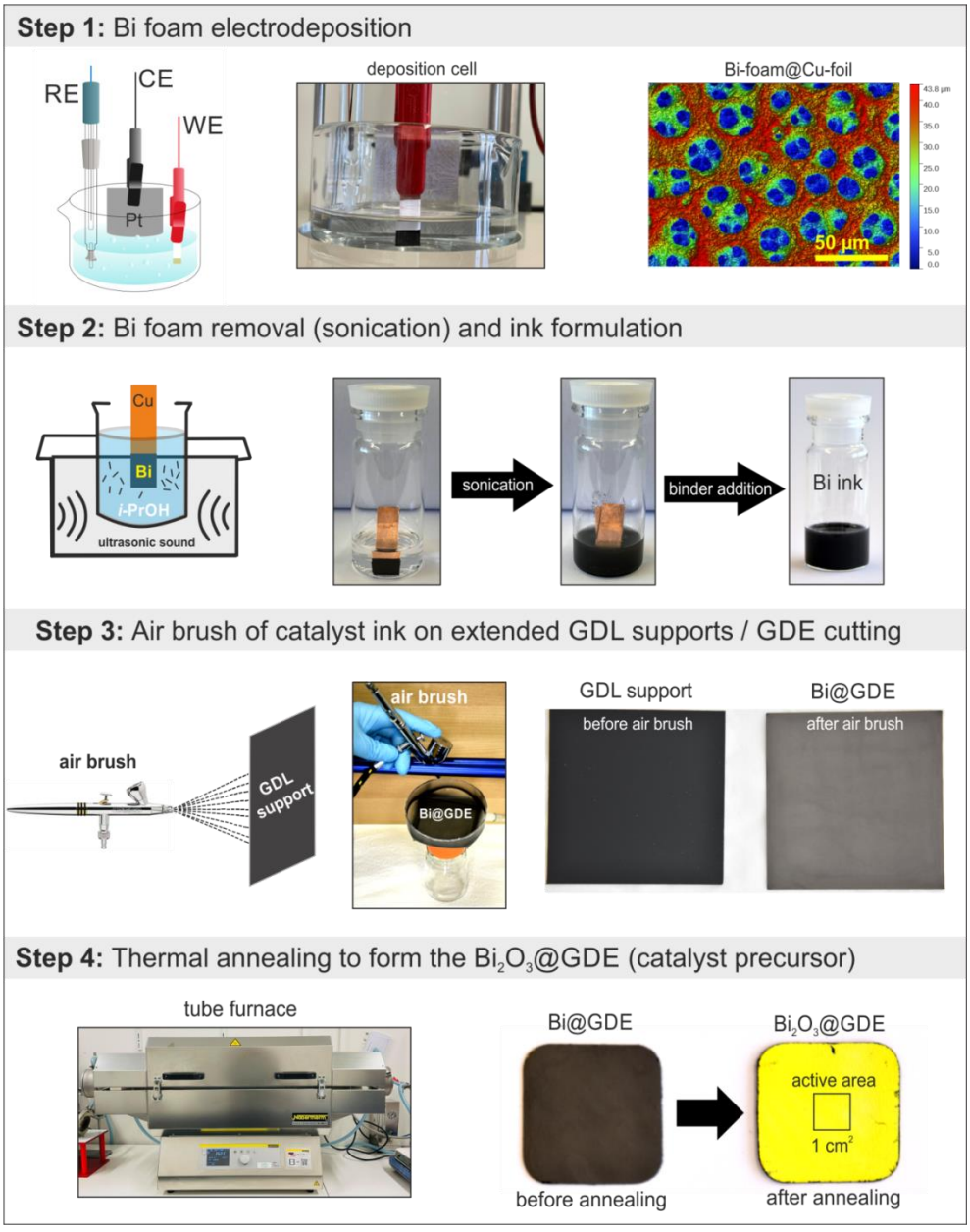
Step 1: Bi foam electrodeposition
RE
CE
WE
Pt
deposition cell
Bi-foam@Cu-foil
50 µm
Step 2: Bi foam removal (sonication) and ink formulation
Cu
Bi
i-PrOH
ultrasonic sound
sonication
binder addition
Bi ink
Step 3: Air brush of catalyst ink on extended GDL supports / GDE cutting
air brush
GDL support
air brush
Bi@GDE
GDL support
before air brush
Bi@GDE
after air brush
Step 4: Thermal annealing to form the Bi2O3@GDE (catalyst precursor)
tube furnace
Bi@GDE
Bi2O3@GDE
active area
1 cm2
before annealing
after annealing

# Figure 4

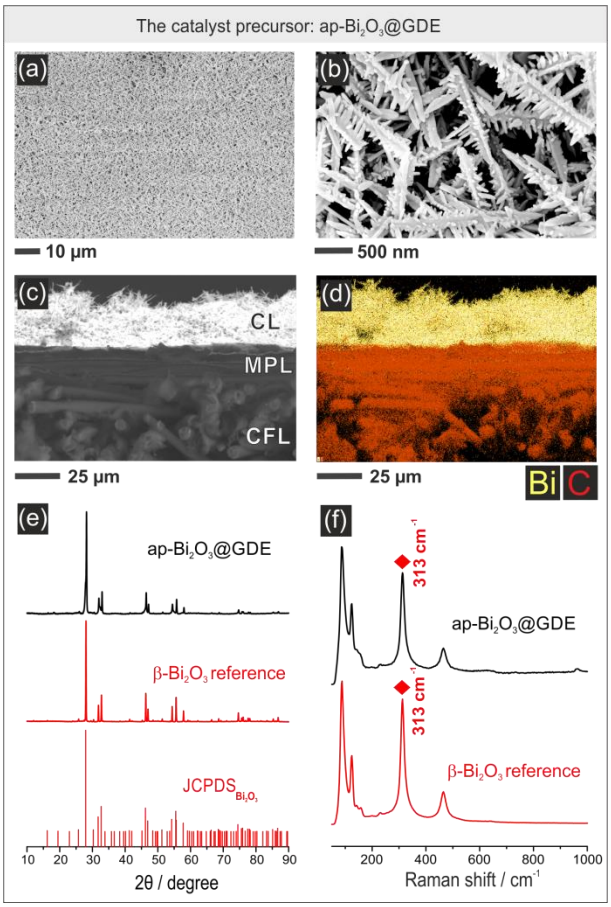
The catalyst precursor: ap-Bi2O3@GDE
(a)
10 μm
(b)
500 nm
(c)
CL
MPL
CFL
25 μm
(d)
25 μm
Bi
C
(e)
ap-Bi2O3@GDE
β-Bi2O3 reference
JCPDSBi2O3
10 20 30 40 50 60 70 80 90
2θ / degree
(f)
313 cm-1
ap-Bi2O3@GDE
313 cm-1
β-Bi2O3 reference
200 400 600 800 1000
Raman shift / cm-1

# Figure 5

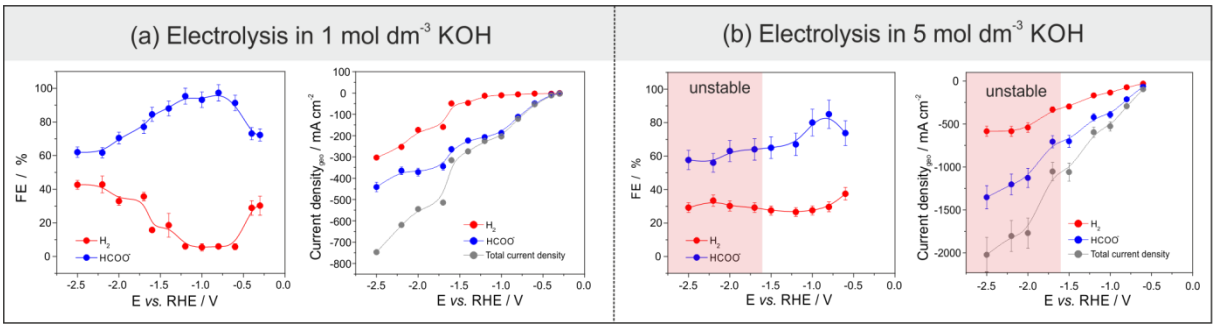
(a) Electrolysis in 1 mol dm-3 KOH
(b) Electrolysis in 5 mol dm-3 KOH
FE / %
E vs. RHE / V
H2
HCOO-
Current densitygeo / mA cm-2
Total current density
unstable

# Figure 6

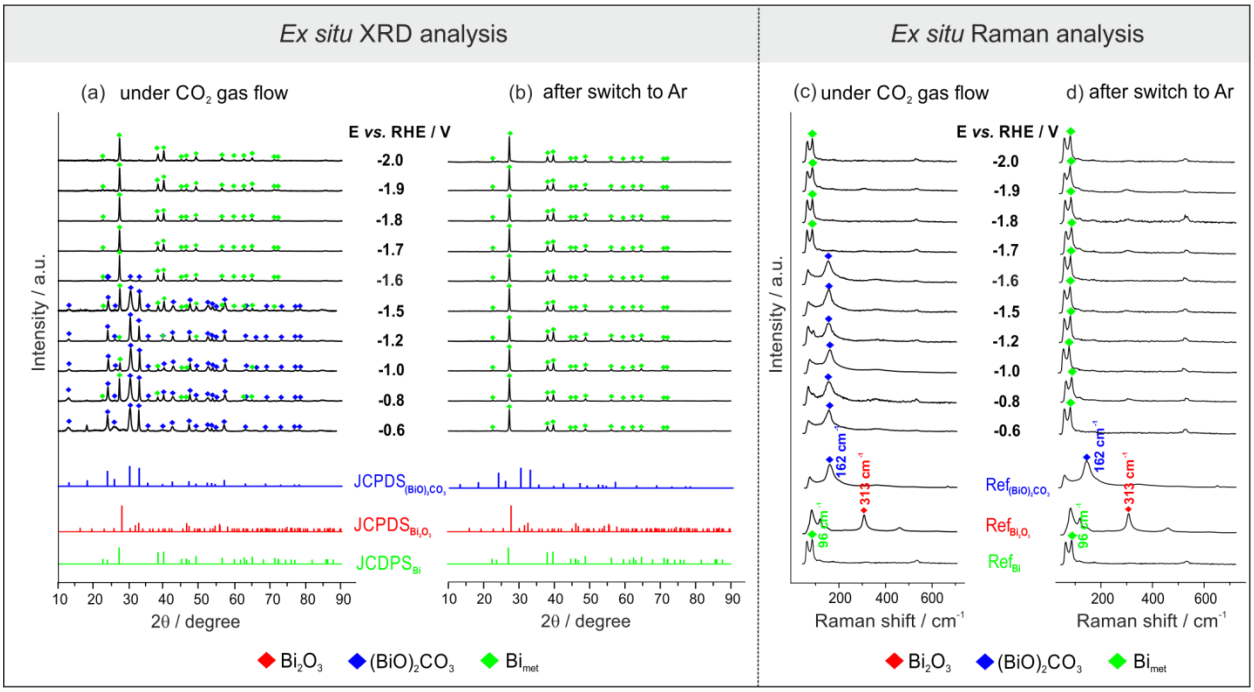
*Ex situ* XRD analysis
*Ex situ* Raman analysis
(a) under $CO_2$ gas flow
(b) after switch to Ar
(c) under $CO_2$ gas flow
d) after switch to Ar
E *vs.* RHE / V
-2.0
-1.9
-1.8
-1.7
-1.6
-1.5
-1.2
-1.0
-0.8
-0.6
Intensity / a.u.
$JCPDS_{(BiO)_2CO_3}$
$JCPDS_{Bi_2O_3}$
$JCDPS_{Bi}$
2θ / degree
Raman shift / $cm^{-1}$
162 $cm^{-1}$
313 $cm^{-1}$
96 $cm^{-1}$
$Ref_{(BiO)_2CO_3}$
$Ref_{Bi_2O_3}$
$Ref_{Bi}$
$Bi_2O_3$
$(BiO)_2CO_3$
$Bi_{met}$

## Figure 7

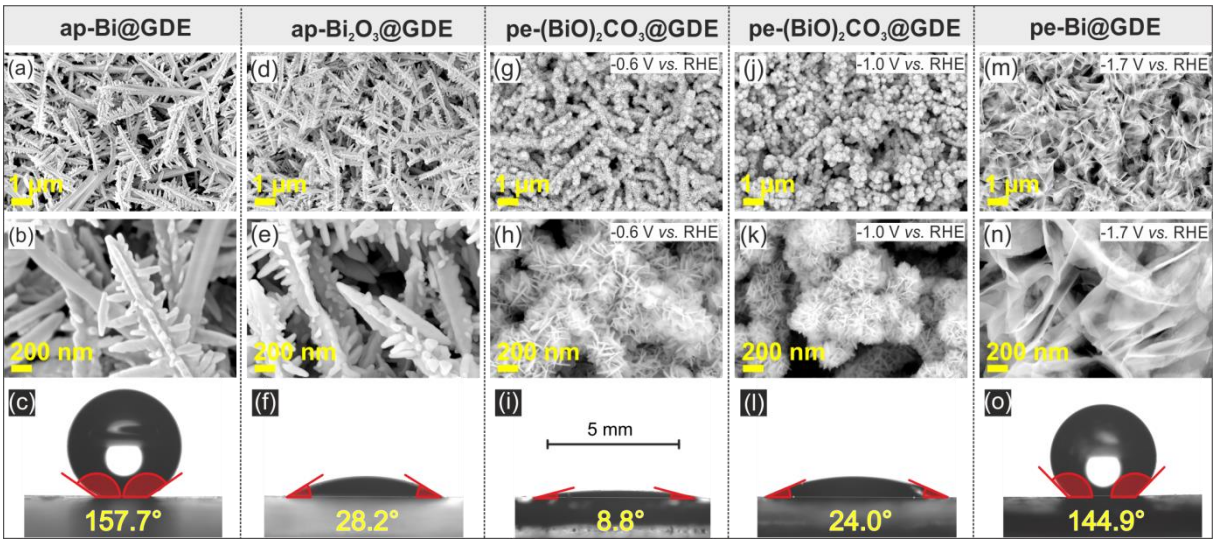
ap-Bi@GDE
ap-Bi2O3@GDE
pe-(BiO)2CO3@GDE
pe-(BiO)2CO3@GDE
pe-Bi@GDE
(a)
(d)
(g)
-0.6 V vs. RHE
(j)
-1.0 V vs. RHE
(m)
-1.7 V vs. RHE
1 μm
(b)
(e)
(h)
-0.6 V vs. RHE
(k)
-1.0 V vs. RHE
(n)
-1.7 V vs. RHE
200 nm
(c)
(f)
(i)
5 mm
(l)
(o)
157.7°
28.2°
8.8°
24.0°
144.9°

## Figure 8

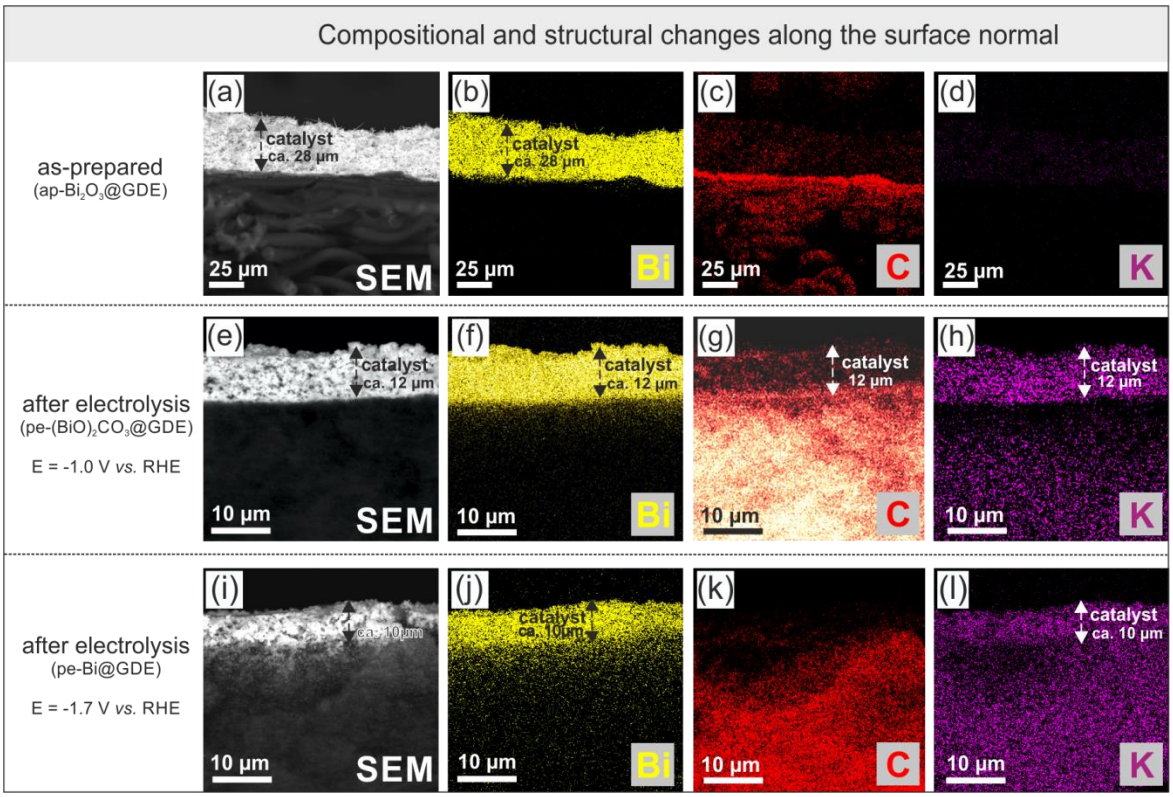
Compositional and structural changes along the surface normal
as-prepared
(ap-Bi2O3@GDE)
after electrolysis
(pe-(BiO)2CO3@GDE)
E = -1.0 V vs. RHE
after electrolysis
(pe-Bi@GDE)
E = -1.7 V vs. RHE
(a)
(b)
(c)
(d)
(e)
(f)
(g)
(h)
(i)
(j)
(k)
(l)
catalyst
ca. 28 µm
ca. 12 µm
ca. 10 µm
12 µm
25 µm
10 µm
SEM
Bi
C
K

**Figure 9**

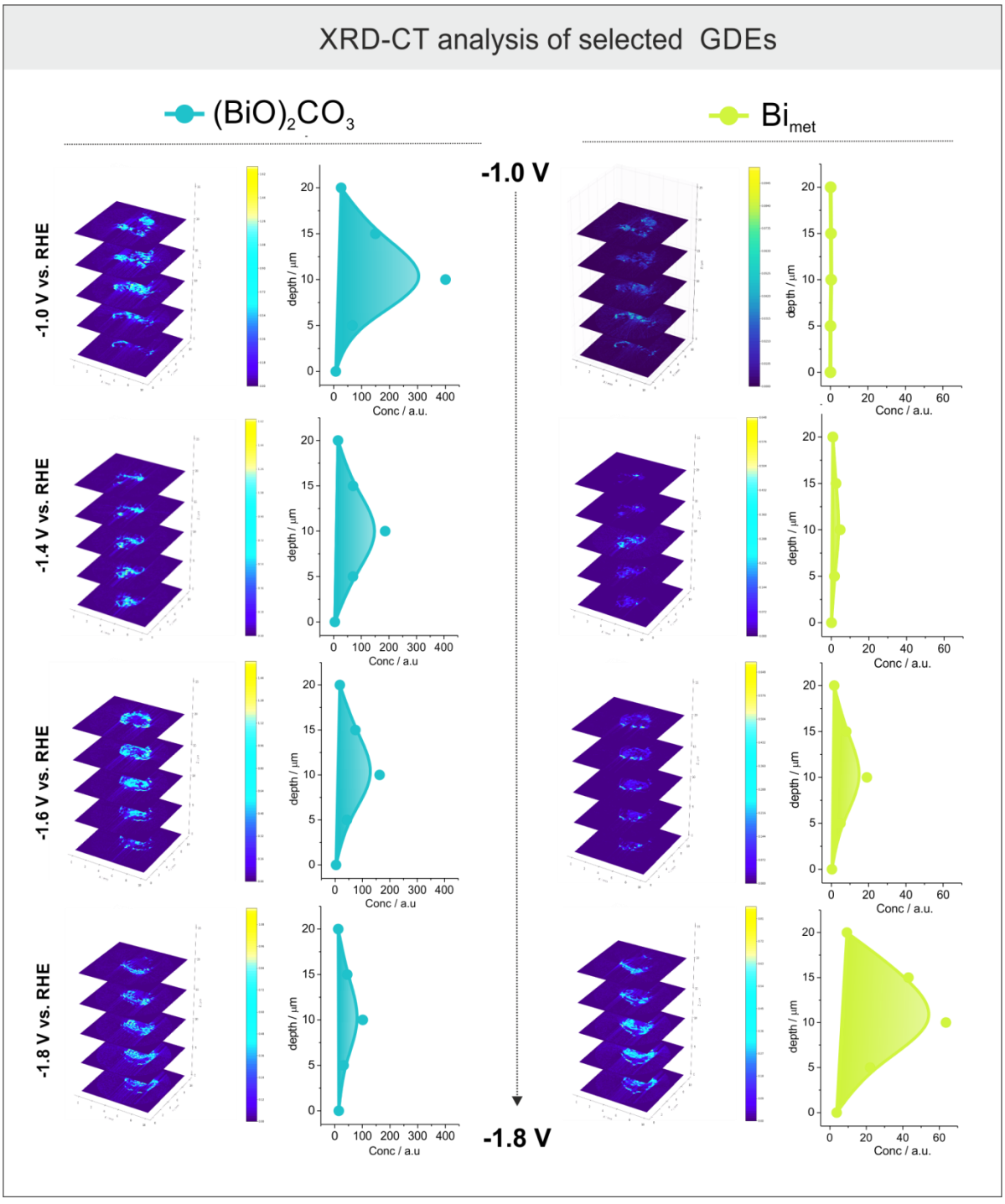
XRD-CT analysis of selected GDEs
(BiO)2CO3
Bimet
-1.0 V
-1.8 V
-1.0 V vs. RHE
-1.4 V vs. RHE
-1.6 V vs. RHE
-1.8 V vs. RHE
depth / µm
Conc / a.u.
Conc / a.u

## Figure 10

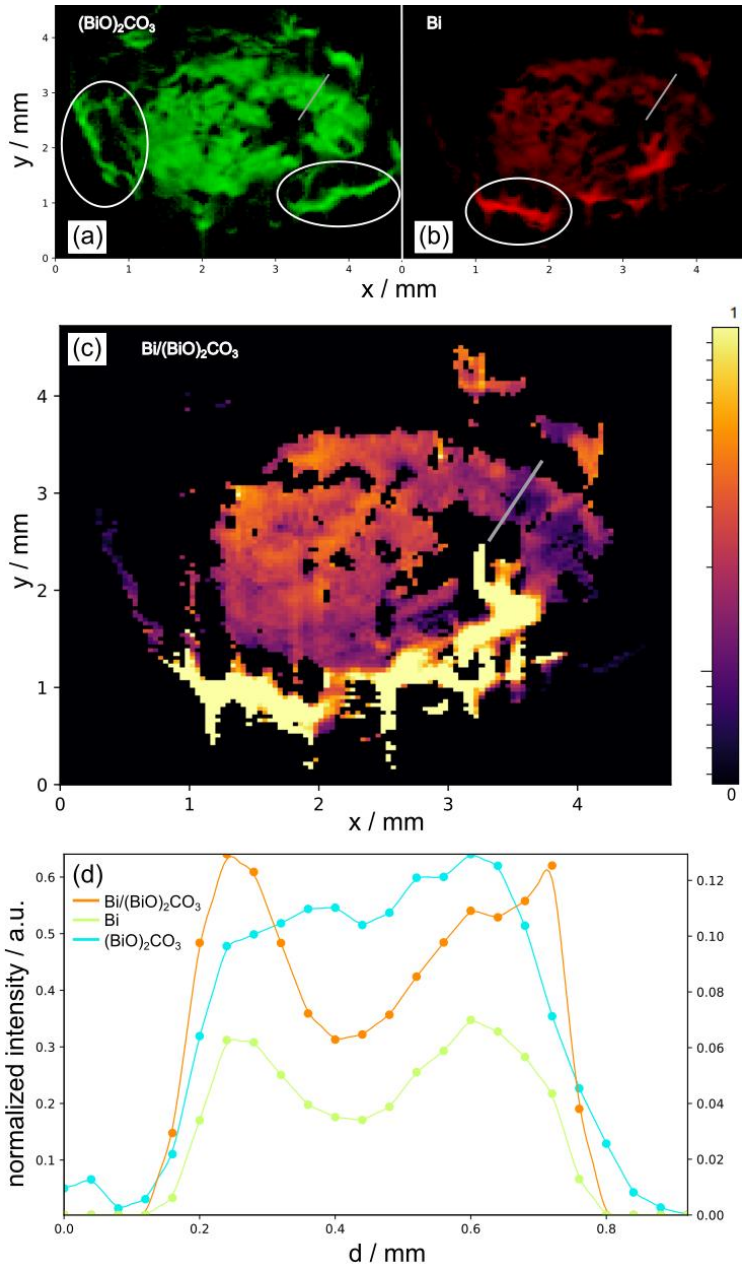
(BiO)2CO3
Bi
(a)
(b)
y / mm
x / mm
(c)
Bi/(BiO)2CO3
1
0
(d)
Bi/(BiO)2CO3
Bi
(BiO)2CO3
normalized intensity / a.u.
d / mm